Hypoxia-Induced Active Dynamics Promotes Early Tumorigenesis

Zhengduo Wang[1], Li Tian[2] and Bo Li[1, *]
1. The Institute for Advanced Studies, Wuhan University, Wuhan 430072, P. R. China.
2. Department of Physics, Wenzhou University, Wenzhou 325000, P. R. China.
* Corresponding author. Email: libo@whu.edu.cn

Abstract: Understanding early tumor formation offers critical insights for cancer prevention at the earliest stages. However, most *in vivo* studies focus on later stages, providing limited information on initial tumorigenesis. Hypoxia, a common physiological condition, is a primary microenvironmental factor in cancer. While molecular studies indicate significant yet sometimes conflicting roles of hypoxia in cancer progression, experimental data on hypoxia's impact on tumor formation from a single cell, especially regarding cellular dynamics, remain scarce. To address this gap, we developed an integrated platform for live-cell imaging under hypoxic conditions, enabling, for the first time, observation of 3D tumor spheroid development from a single cell. Our results show that tumorigenesis is markedly accelerated under hypoxia. Beyond linear growth, we demonstrate that directional movement enhances fusion events, leading to larger spheroids that, in turn, stimulate further proliferation — a positive feedback loop between spheroid dynamics and growth. Actin polymerization and cell-cell adhesion are optimized to promote spheroid fusion. Additionally, hypoxia induces cells with outreaching F-actin co-localized with smaller nuclei to bridge gaps between spheroids, facilitating fusion, while the appearance of tiny nuclei suggests genetic instability. These findings provide direct insights into hypoxia's role in early tumorigenesis, highlighting the potential of modulating dynamic, mechanical, and physiological factors for cancer prevention.

Cancer becomes life-threatening after multiple stages of transformation from normal cells. Hallmarks of advanced stages, such as angiogenesis and metastasis, typically indicate a poorer prognosis [1, 2]. Thus, characterizing tumor features at the earliest stages is critical for early detection and prevention [3, 4]. The prevailing model of early tumorigenesis proposes that mutations give certain cells a survival advantage over their normal neighbors, allowing these transformed cells to proliferate and develop into a primary tumor [5]. Although extensively studied through molecular experiments, this model has not been directly validated. *In vivo* studies on animal models or patient samples primarily use a posterior strategy, analyzing established primary tumors or metastases [6, 7], leaving early tumorigenesis largely unexplored. By contrast, *ex vivo* live-cell imaging platforms offer an opportunity to observe cellular processes from the onset in precisely controlled environments [8, 9] Recent advancements in 3D culture systems now allow for more complex biological processes to be studied *ex vivo* [10, 11] providing new avenues for experimental observation of early tumorigenesis.

Hypoxia, a common physiological condition, constitutes a primary microenvironmental factor for many cells. Oxygen limitation has been implicated in cancer initiation and progression [12-14] Classical hypoxia-inducible factors (HIF) and related signaling pathways [15-17] have documented effects on cell cycle [18], apoptosis [19], immunity check [20], angiogenesis [21], metastasis [22], and resistance to therapy [23]. However, how hypoxia influences early tumorigenesis remains unknown due to a lack of direct experimental evidence. Further, molecular analysis alone does not capture the dynamic changes induced by hypoxia, such as cell movement, fusion, and spatial reorganization—processes crucial in embryo development [24] and cancer metastasis [25]. Along with oxygen scarcity, tumor cells interact with various environmental factors and with each other [26]. Mechanical forces influence tumorigenesis by affecting cell-cell adhesion [27], interactions with the extracellular matrix (ECM) [28], cell migration [29], and cell stiffness [30]; however, the role of these forces under hypoxia remains underexplored [31]. Most research on hypoxia has focused on molecular mechanisms or signaling pathways, leaving the coupling between dynamic, mechanical, and biochemical factors largely unexamined.

The epithelial system accounts for roughly 75% of all cancers [32]. Epithelial cells, which are in constant interaction with the external environment, experience fluctuating physical and chemical conditions that can drive mutations. Given the strong cell-cell communication within epithelia, epithelial tumors arise through multicellular processes. Additionally, with rich connections to blood vessels, immune cells, and the ECM, epithelial tumors can readily metastasize throughout the body. Importantly, early-stage epithelial tumors lack angiogenesis, thus existing in extremely low-oxygen conditions [33]. These characteristics underscore the importance of studying early tumorigenesis of epithelial origin under hypoxic conditions.

To address the current lack of foundational understanding in early tumorigenesis, we developed an integrated platform to capture tumor formation from a few cells. The platform includes several components (**Extended Data Fig. 1**). First, a human kidney-derived tumor cell line, genetically modified for protein visualization, was used to analyze underlying mechanisms (**Fig. S1, Table S1, S2**). The HEK293T cell line, widely utilized in cancer research [10, 34-36] was seeded in a Matrigel suspension, where cells grew as 3D spheroids [10, 11]. The cells occupied a gel matrix with cavities larger than the spheroids, providing weak ECM support for maintaining 3D structure (**Fig. S2**). Notably, only in 3D culture did cancer and cancer stem cell markers express fully (**Extended Data Fig. 2, Fig. S3a, b**), rationalizing the system as a model for tumorigenesis [35, 37]. A spinning-disk confocal microscopy, coupled with three-gas incubator, enabled long-term live-cell imaging with minimal phototoxicity. By adjusting nitrogen gas supply, tumorigenesis was observed under different oxygen conditions, from hypoxia (2%) to normoxia (21%). Finally, live-cell imaging data was analyzed using AI-assisted segmentation (**Fig. S4**) alongside molecular cell biology data (**Figs. S3, S5; Table S3, S4**) to elucidate the mechanisms of early tumorigenesis. Further experimental details are provided in the **Methods** section.

Hypoxia promotes tumorigenesis through active fusion.

After 42 hours of culture, tumor spheroids formed under 2% oxygen were both more numerous and larger

than those grown under normoxic conditions (**Fig. 1a, Supplementary Movie 1**). Quantitative analysis shows a fourfold increase in tumor size and total cell number under hypoxia, with a moderate decrease in spheroid number by 31% (**Fig. 1b**). These results clearly indicate that hypoxia accelerates early tumorigenesis. Two dynamic processes contribute to this effect: fusion between tumor spheroids and growth driven purely by cell proliferation. For both normoxia and hypoxia, fusion accounts for approximately 70% of tumorigenesis, significantly outweighing the ~30% contribution from proliferation alone (**Fig. 1c**). Under hypoxia, fusion frequency doubles (**Fig. 1d, Supplementary Movie 2**), and fusion event duration decreases by 55% (**Fig. 1e, Supplementary Movie 2**), leading to increased tumor size in a shorter time. Fusion events can be further classified into two modes (**Fig. 1f**). In the *active mode*, tumor spheroids move freely within the Matrigel network until their outer surfaces make contact (**Fig. 1e, h, Supplementary Movie 3**). We refer to this as "active fusion". In the *passive mode*, spheroid centers oscillate near their initial positions, and fusion results as a by-product of growth (**Fig. 1e, g, Supplementary Movie 4**). Under hypoxic conditions, active fusion predominates (**Fig. 1f**), indicating that hypoxia drives early tumorigenesis by increasing active spheroid dynamics. Based on these results, we conclude that active fusion events and associated spheroid dynamics are key drivers of enhanced tumorigenesis.

Compared to single, isolated cells, tumor cells within spheroids exhibit enhanced survival in 3D [38, 39], as close cell-cell contacts create a more favorable microenvironment. This improved viability, in turn, promotes both cell dynamics and proliferation, creating a positive feedback loop between active spheroid dynamics and tumorigenesis (**Extended Data Fig. 3**). This hypothesis is supported by time-resolved analysis (**Fig. 1k-n**). Immediately upon hypoxia exposure, spheroid speed increases, validating that spheroid dynamics are central to enhanced tumorigenesis. The immediate effect of active dynamics is to lower barriers to contact, increasing fusion frequency after a brief 6-hour lag. Approximately 10 hours later, proliferation rates begin to increase, reflecting improved cell survival in larger spheroids. Finally, tumor spheroid size shows marked growth after approximately 24 hours, signifying a surge in tumorigenesis (**Fig. 1**). Under normoxia, the initial speed increase is absent, resulting in stable fusion frequency and proliferation rates over time, with slower spheroid growth dominated solely by proliferation (**Fig. 1k**). In contrast, qPCR analysis on HIF1α doesn't exhibit any increase until 48 hours after hypoxia treatment (**Fig. S3d**), far delayed behind the active fusion and enhanced early tumorigenesis. This exclude the possibility that HIF1α being the upstream gene that regulate the active dynamics. Together, these findings highlight the critical role of active fusion in accelerated tumorigenesis and elucidate a sequence of events where active dynamics drive fusion, which in turn promotes growth.

Accompanying the active fusion process, notable heterogeneity in both the dynamics and morphology of spheroids emerges. Under hypoxic conditions, the standard deviations of both spheroid speed and size increase significantly compared to those observed in normoxia (**Fig. 1o, p**). This phenotypic heterogeneity directly reflects the impact of active dynamics. As two spheroids are undergoing active fusion, the dyanamics of them slow down, aligning with the sharp decrease in speed observed approximately 10 hours after hypoxia treatment (**Fig. 1l**). Since not all spheroids undergo fusion, those growing solely through proliferation naturally remain smaller than those formed via active fusion, leading to a broader distribution of spheroid sizes under hypoxia (**Fig. 1p**). Furthermore, this phenotypic heterogeneity likely mirrors underlying genetic diversity.

Quantifying tumor spheroid dynamics reveals key aspects of active fusion. Representative spheroid trajectories (**Fig. 2a-d**) show navigation ranges prior to fusion. Under hypoxia, spheroids become unpinned from their original positions, moving freely in 3D space. Additionally, spheroid speed increases by 57.4 % under hypoxia compared to controls (**Fig. 2e**). Over time, spheroids move away from their initial positions at a higher rate (**Fig. 2f**), allowing fusion to occur over greater distances (**Fig. 2g**). All these dynamic changes collectively enhance fusion frequency. Hints of hypoxia-induced migration was observed in established tumors, in the central region of which necrosis has occurred [40], while it is in a different stage of cancer development compared with the early tumorigenesis in the present work. Remarkably, once an active fusion event begins, the motion of fusing spheroids shifts from a random walk (**Fig. 2h**) to directional movement toward each other (**Fig. 2i**), a phenomenon absent in normoxia (**Fig. 2h**). This suggests that spheroids can detect nearby spheroids and actively engage in fusion. How cells, collectively behaving as a tumor, sense direction and coordinate motion in a homogeneous 3D environment presents a fundamental question in cancer

research. In the following sections, we examine the cellular and molecular mechanisms underlying this directional behavior in tumor spheroids.

The mechanics and morphology of spheroids change during active fusion. Spheroids show reduced circularity under hypoxia (**Fig. 2l**), with greater deformation over similar time periods (**Fig. 2m**). Laser ablation experiments reveal that spheroids undergo higher levels of structural reorganization after the targeted removal of single cells (**Fig. 2n, Supplementary Movie 5**). Nano-indentation measurements show that individual cells within hypoxic spheroids have reduced stiffness (**Extended Data Fig. 4g**). In short, under hypoxia, spheroids adapt their mechanical and morphological properties to enhance dynamics (**Fig. 2e-g**) and shorten fusion time (**Fig. 1e**). These observations indicate a complex interplay between mechanical and dynamic factors during active fusion, whose molecular and structural basis is explored in subsequent sections.

Actin polymerization and cell-cell adhesion are optimized for active fusion.

To elucidate the molecular basis underlying the dynamical-mechanical couplings in active fusion, we manipulated cell mechanics using pharmacological inhibitors (PHAi), RNA interference (RNAi), and overexpression (OE) experiments (**Table S5**). As a key component of the cytoskeleton, actin polymerization—the assembly of actin monomers into filaments—regulates cell polarization [41] and is crucial for dynamic processes like cell migration [42, 43]. In the crucial step of epithelial-to-mesenchymal transition for cancer development, the focus is on the cell-cell adhesion and cell-ECM interaction [44, 45], actin is not reported as the central regulator with equal frequency. Our PHAi experiments, however, show that activating actin polymerization increases both tumor formation rates and fusion frequency, replicating the behavior observed under hypoxia (**Fig. 1c-d, Supplementary Movie 6**). Conversely, inhibiting actin polymerization results in low levels of tumor formation and fusion, even in hypoxic conditions (**Fig. 1c-d, Supplementary Movie 6**). Notably, enhanced actin polymerization has effects on spheroid circularity, fusion time, and phenotypic heterogeneity comparable to hypoxia (**Fig. 1e, o, p, 2l, m**). Chronological analysis of actin PHAi data mirrors the sequence of events under hypoxia, supporting the conclusion that actin polymerization promotes similar spheroid dynamics to those observed in hypoxia (**Fig. 1m, n**). Enhanced actin polymerization is thus identified as the primary mechanical factor driving increased navigation range (**Fig. 2c, d, f, g**), speed (**Fig. 2e**), and directional movement (**Fig. 2j, k**) under hypoxia, enabling tumor spheroids to deform and actively fuse in response to hypoxic conditions. The functional role of actin polymerization in early tumorigenesis observed in the present experiments implies the response of Rho and ROCK pathways under hypoxia [46] although at the time of promoted actin polymerization, no upregulation of HIF1α yet occurs (**Fig. S3d**).

To further assess the roles of cell-cell adhesion and cell-ECM interaction, we performed RNAi and OE manipulations of DSG2 and integrin β-3 (ITGB3), both of which have been reported to be hub modulator in tumorigenesis [47, 48]. Previous molecular studies in 2D culture systems have noticed the correlation between HIF1α and the proteins responsible for cell-cell adhesion and cell-ECM interaction [49-51], but the mechanism of the coupling between the cell dynamics and mechanics remains unclear. Reduced DSG2 expression in normoxic conditions induced hypoxia-like behaviors in tumor spheroids (**Fig. 1c-f, Fig. 2e-g, l-n**), while DSG2 overexpression in hypoxia decreased tumorigenesis rates and shifted spheroid behaviors toward those seen in normoxia (**Fig. 1c-f, Fig. 2e-g, l-n**). These findings suggest that tumor spheroids reduce intercellular adhesion to facilitate greater deformation and enhance dynamics. In contrast, altering integrin expression levels had minimal effect on spheroid behavior in 3D (**Fig. S6**), indicating that cell-ECM interactions play a minor role in this environment. This observation is consistent with the large pore size of Matrigel relative to spheroids, which limits direct cell-ECM contact. In 2D cultures, however, cell-ECM interactions influence both tumorigenesis and active fusion (**Extended Data Fig. 4**), highlighting fundamental differences in dynamical-mechanical couplings between 2D and 3D culture systems.

Transcriptomic data corroborate the findings from PHAi, RNAi, and OE experiments. KEGG pathway enrichment analysis reveals gene clusters upregulated under hypoxia, associated with biological processes, signaling pathways, cytoskeletal dynamics, and molecular function. These clusters contain numerous genes involved in actin polymerization and cell-cell communication, with comparatively few related to cell-ECM

interactions (**Extended Data Fig. 5**). Beyond cell mechanics, clustering analysis reveals that hypoxia concurrently promotes cellular metabolism, cancer-associated signaling molecules, cytoskeletal dynamics, and extracellular matrix remodeling (**Extended Data Fig. 5, Fig. S5b-e**). This implies that metabolic shifts may furnish the energy and structural resources needed to support the enhanced dynamics and mechanical force generation observed under hypoxic conditions. Taken together, these results suggest that cells operate as integrated molecular machines, actively optimizing their biochemical properties crossing length scales in response to the environmental cue of low oxygen availability.

Unlike many soft matter systems [52], the fusion and deformation of tumor spheroids result from complex active adaptations rather than simple equilibrium-based physical properties. In an equilibrium system, greater deformation typically indicates reduced stiffness [53]. Here, however, actin polymerization—which often increases cell stiffness [54] paradoxically leads to enhanced deformation and dynamics (**Fig. 1c-e, Fig. 2e-g, l-n**). *In vitro* tests outside cells show cofilin-mediated F-actin cross-linking balance with the actin polymerization into the most appropriate softness for the enhanced network flexibility [55], implying the involvement of multiple factors for the active dynamics. The controversial outcome has also been reported in the role of E-cadherin under hypoxia [49], which is a crucial adhesive protein between cells. RNAi, PHAi, and OE experiments indicate that each molecule analyzed has an optimal concentration for maintaining spheroid functionality; further increases in actin polymerization or DSG2 knockdown under hypoxia do not enhance active fusion (**Fig. S7**). These molecular findings reveal a finely tuned balance between dynamics and mechanics within tumor spheroid cells.

Outreaching F-actin and Tiny Cells Enable Remote Sensing by Bridging the Fusion Gap.

To uncover the structural mechanisms supporting active fusion, we closely examined the dynamics of the cytoskeleton and cell nuclei. Following hypoxia treatment, a distinct cell type with notably small nuclei emerges within the tumor spheroids (**Fig. 3a-d, Extended Data Fig. 6; Supplementary Movie 7**). These "tiny" cells, with nuclear sizes averaging 23.9 % of that of typical nuclei, are virtually absent under normoxic conditions. The nuclei size distribution shifts to a bimodal pattern under hypoxia, contrasting with the continuous distribution observed in normoxia (**Fig. 3e**). Chromosome immunostaining verifies these tiny nuclei as cellular rather than organelle-like entities (**Fig. 3f**), and their number increase rate is nearly quadruple that of normal cells (**Fig. 3g**). The emergence of distinct nuclear size distribution and number increased rate provide strong evidence that these tiny nuclei represent a novel cell subtype within the tumor spheroid. This adaptation to environmental stress suggests underlying genetic instability, a known hallmark of cancer [56].

Under hypoxic conditions, immunostaining reveals that F-actin forms distinctive outreaching structures connecting adjacent spheroids during fusion (**Fig. 3h-k; Extended Data Fig. 6a-d; Supplementary Movie 8**). This phenomenon is unique to hypoxia, as no comparable structure appears in normoxic conditions (**Fig. 3h, i**). The protruding F-actin have been observed in 3D culture, constituting structures like filopodia to facilitate cell migration [57]. In our experiment, the outreaching F-actin structures are not uniformly distributed around the spheroid but consistently form near the gap between two closely situated spheroids (**Fig. 3j**). The length of these F-actin extensions can rival the spheroid diameter itself (**Fig. 3k**), drastically extending the sensing and communication range of the spheroids under hypoxia relative to normoxia. Super-resolution imaging shows spatial colocalization of the outreaching F-actin with tiny cell nuclei (**Fig. 3j, Extended Data Fig. 6a-d**), with the actin filaments creating channels that bridge the spheroids. Time-lapse imaging captured the dynamic process that the outreaching F-actin forms (**Supplementary Movie 9**). Labeled by live cell dye, it can be observed that the F-actin protrudes out from one spheroid, and elongates in the direction pointing to the other one it fuses with 2-3 hours later (**Extended Data 6e-h)**. Chronological analysis shows that actin elongation occurs simultaneously with spheroid speed up and distance drop during the active fusion, confirming the correlation of these events (**Fig. 3l**). These data prove that the outreaching F-actin facilitates material exchange between spheroids, positioning outreaching F-actin as a structural basis for remote sensing and active fusion.

Further analysis reveals the critical role of tiny cells in active fusion. Spatially, tiny cells localize predominantly near the spheroid surface, in contrast to the homogeneous distribution of normal cells (**Fig. 3m-p**). Notably, these cells cluster at the surface closest to the neighboring spheroid during fusion, effectively bridging the gap (**Fig. 3m, n**), a configuration that distinguishes post-fusion (**Fig. 3o**). The angular probability distribution between the tiny cell's position, the spheroid center, and the axis connecting two spheroids (**Fig. 3q**) statistically validates this clustering tendency observed in live imaging (**Fig. 3m-o**). Additionally, the smaller size of these cells may enable easier passage through the F-actin channels, consistent with *in vitro* studies where cells adaptively migrate through confined spaces by reshaping their nuclei [58, 59]. Tiny cells also exhibit significantly higher motility than normal cells (**Fig. 3r**), likely granting them the flexibility to rapidly adjust their positions within the spheroid.

Targeted ablation of either outreaching F-actin or tiny cells through laser techniques notably reduces tumorigenesis rates under hypoxia (**Extended Data Fig. 7**), underscoring their essential roles in this process. Together, these findings suggest that active spheroid fusion arises from the coordinated actions of the cytoskeleton and nucleus. The outreaching F-actin structures amplify the spheroids' sensing and communication range, while tiny cells at the proximal surface act as "sentinels", traversing F-actin channels and facilitating mass transport. This coordinated system directs the spheroids' movement and promotes active fusion.

Stimulated cell cycle enhances proliferation and spheroid growth.

Following active fusion, the rate of cell proliferation shows a marked increase, indicating a coupling between spheroid dynamics and cell proliferation (**Fig. 1l**). Although cell proliferation-driven growth of the tumor spheroid is less prominent than fusion, it still accounts for approximately 20 % of the overall tumorigenesis rate (**Fig. 1c**). Under hypoxic conditions, this contribution rises by 40 % (**Fig. 1c**), alongside a substantial increase in cell proliferation rate (**Fig. 4b**), underscoring the importance of proliferation-driven growth in tumor spheroid development. In 2D culture, the hypoxia in general results in cell cycle arrest due to the effect of gatekeeper genes like p53 [19, 60], in contrast with the enhanced proliferation observed here in tumor spheroid, raising another fundamental difference between the 3D and 2D systems when modeling tumorigenesis. Compared with the 2D culture in close contact with the substrate, the loss of anchorage with the ECM in 3D or *in vivo* endows the cells with stronger environmental pressure, driving them away from a normal state into a more unstable and proliferative tumor state [61, 62]. This reasoning could also explain why enhanced proliferation was confusingly observed in tumor cells or cancer cells under hypoxia, even in 2D [18, 63-65].

To visualize cell cycle dynamics, we employed the FUCCI technique, enabling precise tracking of cell cycle phases (**Methods**, **Supplementary Materials, Table S2**). Statistical analysis reveals that under hypoxia, the proportion of cells in the S/G2/M phases is approximately 10 % higher than under normoxia (**Fig. 4c**), suggesting a hypoxia-induced acceleration of cell proliferation. Over time, this effect amplifies, with nearly all cells entering the S/G2/M phases after 42 hours of hypoxia exposure (**Fig. 4d, e, h, i; Supplementary Movie 10**). Notably, the rate of increase in the S/G2/M cell proportion is non-linear. Initially, the proportion of cells in G1 and S/G2/M remains stable, but after a critical threshold, the S/G2/M phase proportion begins a linear ascent (**Fig. 4i**), marking a proliferation rate jump confirmed by cell counts (**Fig. 1l**). This analysis supports the hypothesis that larger spheroids, which are better suited for cell survival in 3D culture, stimulate cell proliferation, contributing to overall spheroid growth.

Mechanistically, the stimulation of the cell cycle within the nucleus is linked to cytoskeletal dynamics, echoing previous studies at the molecular level [66]. When actin polymerization is activated, the proportion of cells in S/G2/M phases increases, even in the absence of hypoxia (**Fig. 4j**). Conversely, inhibiting actin polymerization prevents this increase in S/G2/M phase cells under hypoxia (**Fig. 4k**). Tiny cells, which number increase at a rate four times that of normal cells, fail to form when actin polymerization is suppressed (**Fig. 3e**). Thus, in addition to hypoxia, specific cytoskeletal conditions are essential for the generation of tiny

cells and the enhanced proliferation they drive. Remarkably, genetic instability within tumor spheroids appears to be modulated by cytoskeletal mechanics, linking external mechanical properties to nuclear behavior.

The immunostaining of p53 unravels the molecular mechanism for the stimulated cell cycle (**Fig. 4l-n**). Being a guardian gene that steers DNA repair, p53 is widely involved in cancer development [32]. Under hypoxia, p53 has been documented to be a transcriptional factor that is responsible for cell cycle arrest, apoptosis, and metastasis [19, 60], although its role in tumorigenesis can be controversial for different cells [60, 64]. Under normoxia, p53 is co-localized with the nucleus in most of the cells (**Fig. 4l**), indicating the self-defense mechanism in the tumor cells is activated to prevent further DNA damage and transformation to cancer cells. In contrast, p53 is absent in the nucleus under hypoxia (**Fig. 4m**) except those of the tiny cells (**Fig. 4n**). On average, the percentage of $p53^+$ cells in hypoxia reduced by almost three times compared with that of normoxia (**Fig. 4o**). Without the restriction of p53 at the cell cycle checkpoint, the proliferation is unlimited, contributing to larger spheroids.

The percentage of $p53^+$ nucleus for the tiny cells is tremendously high under hypoxia, being almost four times the average value for the normal cells (**Fig. 4p**). This observation proves that the tumor cell lineage diverges into groups with different genetic features under the pressure of hypoxia – the $p53^+$ normal cells and the $p53^-$ tiny cells. The fact that p53 localizes more frequently in the nucleus of tiny cells suggests that these cells underwent more severe DNA damage compared with the normal ones. As p53 usually results in cell cycle arrest, the number increase of the tiny cells cannot come from the proliferation by themselves. Therefore, the tiny cells are more likely to be the product of normal cells with abnormal mitosis, implying genetic instability at the chromosome level [67, 68].

Cell proliferation, therefore, operates as an integral component of spheroid dynamics. Under hypoxia, active fusion is followed by a rapid increase in cell number (**Fig. 1l**), with larger spheroids providing a supportive environment for cell survival and proliferation, further accelerating spheroid growth. As a consequence, the cell cycle is regulated by p53, resulting in both the enhanced proliferation rate (**Fig. 4b**) and the emergence of tiny cells. The tiny cells contribute structurally to fusion by bridging spheroids with outreaching F-actin channels (**Fig. 3j, k**). The enhanced proliferation rate supports a larger population of tiny cells, in turn facilitating active fusion. In summary, the positive feedback between spheroid dynamics and cell proliferation fosters both active fusion and growth, jointly enhancing tumorigenesis under hypoxia.

Summary and Discussion

In summary, this study provides novel experimental insights into how hypoxia accelerates early tumorigenesis. Our observations reveal that actin polymerization extends outward, bridging gaps between spheroids, while tiny nuclei move along F-actin channels, enabling material exchange. This spatial-temporal reorganization of proteins at the cellular level establishes the structural foundation for active fusion and deformation at the spheroid level, ultimately contributing to an elevated rate of tumorigenesis. This process showcases complex interactions among spheroid dynamics, cytoskeletal mechanics, cell cycle kinetics, and molecular signaling. Rather than identifying a singular signaling pathway, our transcriptomic analysis uncovers thousands of genes with differential expression between hypoxic and normoxic samples (**Extended Data Fig.5**), lending strong support to a model of dynamo-mechano-physio-coupling. These findings not only challenge traditional linear models of early tumorigenesis that often reduce it to simple proliferation and growth, but also offering potential therapeutic strategy aiming at the dynamo-mechano-physio-coupling, in addition to those targeting classical signal pathways [69] or microenvironment [70].

Our experiments also underscore the differences between three-dimensional (3D) and two-dimensional (2D) systems, which have also been noticed by molecular studies [35, 61]. Although both share some phenotypic similarities (**Extended Data Fig. 4**), transcriptomic data show that key cancer markers are predominantly expressed in 3D cultures (**Extended Data Fig. 2**), and tiny cells—indicators of genetic instability—emerge only in 3D environments. This finding suggests that 3D culture may better replicate the tumorigenesis process, supporting its use as a closer approximation of *in vivo* conditions. PHAi and RNAi experiments further

demonstrate that cells adapt differently to hypoxia in 3D compared to 2D cultures (**Fig. 2, Extended Data Fig. 4**), reinforcing the importance of 3D models for studying hypoxia-driven processes in cancer research.

These findings also raise new research questions, particularly concerning the molecular mechanisms underlying the observed dynamic processes. Dynamics, a concept typically outside the focus of molecular cell biology, proves critical for understanding functional behaviors in this context. For instance, the transcriptomic analysis fails to identify classical signaling pathways in existing databases (**Fig. S5**), although chemical hypoxia-induced by $CoCl_2$ replicates similar spheroid behaviors (**Fig. S8**). This suggests that integrating dynamic phenotypes from live cell imaging with traditional molecular cell biology methods will require interdisciplinary approaches, merging physical and biological sciences to elucidate these complex processes.

The appearance of tiny cells, signifying genetic instability in response to the microenvironment, is particularly notable. The substantial reduction in nuclear size likely reflects significant genomic alterations, potentially involving whole-chromosome losses or damage [71]. The heightened dynamics of the tiny cells reflect the broader speed distribution of spheroid observed under hypoxia (**Fig. 1o**), suggesting a correlation between genetic and phenotypic heterogeneity. Remarkably, hypoxia-induced genetic instability occurs at such an early stage of tumorigenesis, underscoring its role in the progression of cancer. Future research should explore the biological roles of tiny cells and their potential involvement in later stages of cancer development, such as metastasis.

1. Hanahan, D. & Weinberg, R. A. The hallmarks of cancer. *Cell* **100**, 57-70 (2000).
2. Hanahan, D. & Weinberg, R. A. Hallmarks of cancer: the next generation. *Cell* **144**, 646-674 (2011).
3. Crosby, D. *et al.* Early detection of cancer. *Science* **375**, eaay9040 (2022).
4. Unger-Saldaña, K. Challenges to the early diagnosis and treatment of breast cancer in developing countries. *World J Clin Oncol* **5**, 465-477 (2014).
5. Klein, C. A. Parallel progression of primary tumours and metastases. *Nat Rev Cancer* **9**, 302-312 (2009).
6. Olson, B., Li, Y., Lin, Y., Liu, E. T. & Patnaik, A. Mouse Models for Cancer Immunotherapy Research. *Cancer Discov* **8**, 1358-1365 (2018).
7. Bhandari, V. *et al.* Molecular landmarks of tumor hypoxia across cancer types. *Nat Genet* **51**, 308-318 (2019).
8. Chen, J., Poskanzer, K. E., Freeman, M. R. & Monk, K. R. Live-imaging of astrocyte morphogenesis and function in zebrafish neural circuits. *Nat Neurosci* **23**, 1297-1306 (2020).
9. Domingo-Muelas, A. *et al.* Human embryo live imaging reveals nuclear DNA shedding during blastocyst expansion and biopsy. *Cell* **186**, 3166-3181.e3118 (2023).
10. Le, A. *et al.* Tumorigenicity of hypoxic respiring cancer cells revealed by a hypoxia-cell cycle dual reporter. *Proc Natl Acad Sci U S A* **111**, 12486-12491 (2014).
11. Riffle, S., Pandey, R. N., Albert, M. & Hegde, R. S. Linking hypoxia, DNA damage and proliferation in multicellular tumor spheroids. *BMC Cancer* **17**, 338 (2017).
12. Mohyeldin, A., Garzón-Muvdi, T. & Quiñones-Hinojosa, A. Oxygen in stem cell biology: a critical component of the stem cell niche. *Cell Stem Cell* **7**, 150-161 (2010).
13. Bristow, R. G. & Hill, R. P. Hypoxia and metabolism. Hypoxia, DNA repair and genetic instability. *Nat Rev Cancer* **8**, 180-192 (2008).
14. Gilkes, D. M., Semenza, G. L. & Wirtz, D. Hypoxia and the extracellular matrix: drivers of tumour metastasis. *Nat Rev Cancer* **14**, 430-439 (2014).
15. Keith, B., Johnson, R. S. & Simon, M. C. HIF1α and HIF2α: sibling rivalry in hypoxic tumour growth and progression. *Nat Rev Cancer* **12**, 9-22 (2011).
16. Dang, C. V., Kim, J. W., Gao, P. & Yustein, J. The interplay between MYC and HIF in cancer. *Nat Rev Cancer* **8**, 51-56 (2008).
17. Wouters, B. G. & Koritzinsky, M. Hypoxia signalling through mTOR and the unfolded protein response

390 in cancer. *Nat Rev Cancer* **8**, 851-864 (2008).
391 18. Hubbi, M. E. *et al.* Cyclin-dependent kinases regulate lysosomal degradation of hypoxia-inducible factor
392 1α to promote cell-cycle progression. *Proc Natl Acad Sci U S A* **111**, E3325-3334 (2014).
393 19. Hubbi, M. E. & Semenza, G. L. Regulation of cell proliferation by hypoxia-inducible factors. *Am J*
394 *Physiol Cell Physiol* **309**, C775-782 (2015).
395 20. Park, J. H. *et al.* Tumor hypoxia represses γδ T cell-mediated antitumor immunity against brain tumors.
396 *Nat Immunol* **22**, 336-346 (2021).
397 21. Befani, C. & Liakos, P. The role of hypoxia-inducible factor-2 alpha in angiogenesis. *J Cell Physiol* **233**,
398 9087-9098 (2018).
399 22. Rankin, E. B. & Giaccia, A. J. Hypoxic control of metastasis. *Science* **352**, 175-180 (2016).
400 23. Ma, S. *et al.* Hypoxia induces HIF1α-dependent epigenetic vulnerability in triple negative breast cancer
401 to confer immune effector dysfunction and resistance to anti-PD-1 immunotherapy. *Nat Commun* **13**,
402 4118 (2022).
403 24. Shahbazi, M. N., Siggia, E. D. & Zernicka-Goetz, M. Self-organization of stem cells into embryos: A
404 window on early mammalian development. *Science* **364**, 948-951 (2019).
405 25. Stuelten, C. H., Parent, C. A. & Montell, D. J. Cell motility in cancer invasion and metastasis: insights
406 from simple model organisms. *Nat Rev Cancer* **18**, 296-312 (2018).
407 26. Mishra, D. & Banerjee, D. Metabolic Interactions Between Tumor and Stromal Cells in the Tumor
408 Microenvironment. *Adv Exp Med Biol* **1350**, 101-121 (2021).
409 27. Labernadie, A. *et al.* A mechanically active heterotypic E-cadherin/N-cadherin adhesion enables
410 fibroblasts to drive cancer cell invasion. *Nat Cell Biol* **19**, 224-237 (2017).
411 28. Hamidi, H. & Ivaska, J. Every step of the way: integrins in cancer progression and metastasis. *Nat Rev*
412 *Cancer* **18**, 533-548 (2018).
413 29. Bera, K. *et al.* Extracellular fluid viscosity enhances cell migration and cancer dissemination. *Nature* **611**,
414 365-373 (2022).
415 30. Fiore, V. F. *et al.* Mechanics of a multilayer epithelium instruct tumour architecture and function. *Nature*
416 **585**, 433-439 (2020).
417 31. Wirtz, D., Konstantopoulos, K. & Searson, P. C. The physics of cancer: the role of physical interactions
418 and mechanical forces in metastasis. *Nat Rev Cancer* **11**, 512-522 (2011).
419 32. Weinberg, R. The Biology of Cancer. (2006).
420 33. Vaupel, P., Schlenger, K., Knoop, C. & Höckel, M. Oxygenation of human tumors: evaluation of tissue
421 oxygen distribution in breast cancers by computerized O2 tension measurements. *Cancer Res* **51**, 3316-
422 3322 (1991).
423 34. Stepanenko, A. A. & Dmitrenko, V. V. HEK293 in cell biology and cancer research: phenotype, karyotype,
424 tumorigenicity, and stress-induced genome-phenotype evolution. *Gene* **569**, 182-190 (2015).
425 35. Debeb, B. G. *et al.* Characterizing cancer cells with cancer stem cell-like features in 293T human
426 embryonic kidney cells. *Mol Cancer* **9**, 180 (2010).
427 36. Shen, C. *et al.* The tumorigenicity diversification in human embryonic kidney 293 cell line cultured in
428 vitro. *Biologicals* **36**, 263-268 (2008).
429 37. Keith, B. & Simon, M. C. Hypoxia-inducible factors, stem cells, and cancer. *Cell* **129**, 465-472 (2007).
430 38. Aceto, N. *et al.* Circulating tumor cell clusters are oligoclonal precursors of breast cancer metastasis. *Cell*
431 **158**, 1110-1122 (2014).
432 39. Cheung, K. J. & Ewald, A. J. A collective route to metastasis: Seeding by tumor cell clusters. *Science*
433 **352**, 167-169 (2016).
434 40. Singh, M. *et al.* Targeting the Temporal Dynamics of Hypoxia-Induced Tumor-Secreted Factors Halts
435 Tumor Migration. *Cancer Res* **79**, 2962-2977 (2019).
436 41. Li, R. & Gundersen, G. G. Beyond polymer polarity: how the cytoskeleton builds a polarized cell. *Nat*

Rev Mol Cell Biol **9**, 860-873 (2008).
42. Chen, X. *et al.* Polymerization force-regulated actin filament-Arp2/3 complex interaction dominates self-adaptive cell migrations. *Proc Natl Acad Sci U S A* **120**, e2306512120 (2023).
43. Inagaki, N. & Katsuno, H. Actin Waves: Origin of Cell Polarization and Migration? *Trends Cell Biol* **27**, 515-526 (2017).
44. Loh, C. Y. *et al.* The E-Cadherin and N-Cadherin Switch in Epithelial-to-Mesenchymal Transition: Signaling, Therapeutic Implications, and Challenges. *Cells* **8** (2019).
45. Kariya, Y., Oyama, M., Suzuki, T. & Kariya, Y. αvβ3 Integrin induces partial EMT independent of TGF-β signaling. *Commun Biol* **4**, 490 (2021).
46. Leong, H. S. & Chambers, A. F. Hypoxia promotes tumor cell motility via RhoA and ROCK1 signaling pathways. *Proc Natl Acad Sci U S A* **111**, 887-888 (2014).
47. Qin, S. *et al.* DSG2 expression is correlated with poor prognosis and promotes early-stage cervical cancer. *Cancer Cell Int* **20**, 206 (2020).
48. Zhu, C. *et al.* ITGB3/CD61: a hub modulator and target in the tumor microenvironment. *Am J Transl Res* **11**, 7195-7208 (2019).
49. Chu, K., Boley, K. M., Moraes, R., Barsky, S. H. & Robertson, F. M. The paradox of E-cadherin: role in response to hypoxia in the tumor microenvironment and regulation of energy metabolism. *Oncotarget* **4**, 446-462 (2013).
50. Koike, T. *et al.* Hypoxia induces adhesion molecules on cancer cells: A missing link between Warburg effect and induction of selectin-ligand carbohydrates. *Proc Natl Acad Sci U S A* **101**, 8132-8137 (2004).
51. Donato, C. *et al.* Hypoxia Triggers the Intravasation of Clustered Circulating Tumor Cells. *Cell Rep* **32**, 108105 (2020).
52. Bi, D., Lopez, J. H., Schwarz, J. M. & Manning, M. L. A density-independent rigidity transition in biological tissues. *Nature Physics* **11**, 1074-1079 (2015).
53. Levental, I., Georges, P. C. & Janmey, P. A. Soft biological materials and their impact on cell function. *Soft Matter* **3**, 299-306 (2007).
54. Stricker, J., Falzone, T. & Gardel, M. L. Mechanics of the F-actin cytoskeleton. *J Biomech* **43**, 9-14 (2010).
55. Sun, Z. G. & Murrell, M. Cofilin-Mediated Filament Softening and Crosslinking Counterbalance to Enhance Actin Network Flexibility. *Phys Rev Lett* **133**, 218402 (2024).
56. Lengauer, C., Kinzler, K. W. & Vogelstein, B. Genetic instabilities in human cancers. *Nature* **396**, 643-649 (1998).
57. Caswell, P. T. & Zech, T. Actin-Based Cell Protrusion in a 3D Matrix. *Trends Cell Biol* **28**, 823-834 (2018).
58. Renkawitz, J. *et al.* Nuclear positioning facilitates amoeboid migration along the path of least resistance. *Nature* **568**, 546-550 (2019).
59. Reversat, A. *et al.* Cellular locomotion using environmental topography. *Nature* **582**, 582-585 (2020).
60. Carmeliet, P. *et al.* Role of HIF-1alpha in hypoxia-mediated apoptosis, cell proliferation and tumour angiogenesis. *Nature* **394**, 485-490 (1998).
61. Kim, J. W., Ho, W. J. & Wu, B. M. The role of the 3D environment in hypoxia-induced drug and apoptosis resistance. *Anticancer Res* **31**, 3237-3245 (2011).
62. Nelson, D. A. *et al.* Hypoxia and defective apoptosis drive genomic instability and tumorigenesis. *Genes Dev* **18**, 2095-2107 (2004).
63. Sasabe, E., Tatemoto, Y., Li, D., Yamamoto, T. & Osaki, T. Mechanism of HIF-1alpha-dependent suppression of hypoxia-induced apoptosis in squamous cell carcinoma cells. *Cancer Sci* **96**, 394-402 (2005).
64. Graeber, T. G. *et al.* Hypoxia-mediated selection of cells with diminished apoptotic potential in solid tumours. *Nature* **379**, 88-91 (1996).

65. Ebright, R. Y. *et al.* HIF1A signaling selectively supports proliferation of breast cancer in the brain. *Nat Commun* **11**, 6311 (2020).
66. Provenzano, P. P. & Keely, P. J. Mechanical signaling through the cytoskeleton regulates cell proliferation by coordinated focal adhesion and Rho GTPase signaling. *J Cell Sci* **124**, 1195-1205 (2011).
67. Kondoh, M. *et al.* Hypoxia-induced reactive oxygen species cause chromosomal abnormalities in endothelial cells in the tumor microenvironment. *PLoS One* **8**, e80349 (2013).
68. Duijf, P. H. & Benezra, R. The cancer biology of whole-chromosome instability. *Oncogene* **32**, 4727-4736 (2013).
69. Wilson, W. R. & Hay, M. P. Targeting hypoxia in cancer therapy. *Nat Rev Cancer* **11**, 393-410 (2011).
70. Singleton, D. C., Macann, A. & Wilson, W. R. Therapeutic targeting of the hypoxic tumour microenvironment. *Nat Rev Clin Oncol* **18**, 751-772 (2021).
71. Jevtić, P., Edens, L. J., Vuković, L. D. & Levy, D. L. Sizing and shaping the nucleus: mechanisms and significance. *Curr Opin Cell Biol* **28**, 16-27 (2014).

Methods.

Cell line maintenance and culture. HEK293T (ATCC) cells were grown in DMEM (Adamas life, C8013-500mL) supplemented with 10% heat-inactivated FBS (Gibco). Cells were maintained in an incubator at 37 °C and 5 % CO2 and passaged every 2 to 3 days. Before imaging, the medium was changed or PHAi treatments were applied according to experimental requirements, including DMSO (Adamas Life, 75927AA, 30 μM), Rho Activator II (Cytoskeleton, Cat. # CN03, 2 μg/mL), or Y-27632 (Yesen, 53006ES08, 30 μM). The prepared cell samples were then transferred to a live-cell workstation, where confocal imaging was performed. The mycoplasma testing was conducted weekly on the cell lines using the Mycoplasma Detection Kit (Solea, CA1080). We use Corning Matrigel (356234-5mL) to create a 3D culture environment that assists the tumor cell in forming spheroids [72, 73]. After thawing the Matrigel according to the manufacturer's recommendations, mix it thoroughly with a pipette to ensure homogeneity. Dilute the Matrigel to a 50% concentration with a serum-free medium. Then pour the diluted Matrgel on the confocal dish and incubate at 37°C for 15 minutes to allow solidification. Finally, seed the cells on the confocal dish with solidified Matrigel and add complete culture medium.

Pharmaceutical interference experiment. Rho Activator II (CN03) from Cytoskeleton [74, 75], is stored in a desiccated state at 4°C for no more than 6 months. For reconstitution, briefly centrifuge to collect the product at the bottom of the tube and resuspend each vial in 200 μl of sterile water, place on ice for 10 minutes prior to mixing, and mix by gently pipetting up and down to yield a concentration of 0.1 μg/μl. During use, the compound was diluted in a culture medium to achieve a final concentration of 2 μg/mL for cell treatment. Y-27632 was purchased from Yeasen Biotechnology and is provided as a powder with a purity exceeding 98 % [76, 77]. The powder should be aliquoted and stored at -20 °C dry environment for no more than 2 years. To prepare a stock solution, 10 mg of Y-27632 was dissolved in 312 μL of DMSO to create a 100 mmol/L solution, which was then diluted 10-fold with DMSO to achieve a concentration of 10 mmol/L. This solution was stored at -20 °C. For cell treatment, the solution was further diluted in culture medium to a final concentration of 30 μM.

Construction of monoclonal genetically modified cell lines. We utilized overexpression lentiviral vectors to add fluorescent signals to the target protein for visualization imaging [78], RNA interference [79-83], and of target proteins [84]. The lentiviral vectors used in this study were constructed and synthesized by GeneChem [85]. We packaged the synthesized vectors into lentivirus. The GeneChem lentiviral system consists of the GV lentiviral vector series, pHelper 1.0, and pHelper 2.0 plasmids. After mixing the plasmids,

we performed transient transfection into HEK293T cells using the E-trans DNA transfection reagent (GeneChem, 10038555). Following gentle mixing, the cells were incubated for 48 hours, and the supernatant was collected. Lentivirus was purified using the GeneChem lentiviral particle purification kit and stored at -80 °C. The day before infection, cells were counted and approximately 10,000 cells were seeded in a 12-well plate. After overnight culture, the virus was diluted in serum-free medium and added to the plate to infect the cells at a recommended MOI. After 12 hours, the virus-containing solution was removed, and a complete medium was added for cell culture. After 48 hours, fluorescence intensity was observed under a fluorescence microscope. Corresponding antibiotics were added for cell selection, and monoclones were picked for subsequent experiments. Five stable cell lines are constructed for this study: HEK293T-LifeAct-H2B to visualize F-actin and H2B, HEK293T-FUCCI to visualize cell cycle, HEK293T-DSG2^{OE} to overexpress DSG2, HEK293T-DSG2^{RNAi} to knockdown DSG2, and HEK293T-ITGB3^{RNAi} to knockdown ITGB3. More details about the construction procedure and characteristics of the cell lines are offered in the **Supplementary Information**.

Immunostaining Experiments. For the samples in 3D, the culture medium was aspirated, and the samples were-washed with PBS. They were then fixed at room temperature with 0.4 % glutaraldehyde (National Medicines, 30092436) for 15 minutes, followed by another wash with PBS. Next, the samples were treated with 0.1 % sodium borohydride (Kemiou, 80115818KMO) at 4 °C for one hour to eliminate the effects of glutaraldehyde on imaging. After washing with PBS again, the samples were permeabilized at room temperature with 0.1 % Triton X-100 (Solarbio, T8200-500ml) for 30 minutes. They were then blocked at room temperature for 2 hours using a solution of 3% BSA (Pumeike, PMK0181-250g) prepared in 0.1 % Triton X-100. The samples were incubated overnight at 4°C in the dark with Alexa Fluor™ 488 phalloidin (Thermo Fisher, A12379) diluted 2000-fold in 3 % BSA for actin [86]. The p53 primary antibody (Abcam, catalog no. ab26) was diluted 500-fold with 3 % BSA. The diluted antibody was incubated with the 3D samples overnight at 4 °C. On the following day, the p53 antibody was removed, and the samples were washed three times with PBS, each wash lasting 10 minutes. The Goat anti-Mouse IgG (H+L) secondary antibody was then diluted 1000-fold in 3% BSA and incubated with the samples for 4 hours at room temperature in the dark. Finally, the samples were washed three times with PBS, each wash lasting 10 minutes [87, 88]. After washing twice with PBS, Hoechst 33258 (Pumei Biological, PMK0965) was added for a 30-minute incubation at room temperature to stain the DNA [89]. For the samples in 2D, the culture medium was aspirated and washed once with PBS. They were then fixed at room temperature with 4% paraformaldehyde (Pumei Biological, PMK2040) for 15 minutes, followed by another wash with PBS. The samples were permeabilized at room temperature with 0.5% Triton X-100 (Solarbio, T8200-500ml) for 10 minutes and then washed again with PBS. Next, a blocking solution of 3% BSA (Pumei Biological, PMK0181-250g) prepared in PBS was applied for 1 hour at room temperature. The samples were then incubated overnight at 4 °C in the dark with Alexa Fluor™ 488 phalloidin (Thermo Fisher, A12379), diluted 2000-fold in 3 % BSA. After washing twice with PBS, an anti-fade mounting medium containing DAPI (Pumei Biological, PMK0272) was added, and the samples were incubated at room temperature for 15 minutes before imaging.

Live cell dye staining experiments. SiR-actin (CY-SC001, Cytoskeleton) is a fluorescent probe based on Silicon Rhodamine (SiR) conjugated with the actin-binding natural product Jasplakinolide. This combination enables specific and low-background labeling of F-actin in live cells [90]. Hoechst 33258 was diluted 1000-fold in culture medium and incubated at 37 °C for 1 hour [89]. A 1 mM SiR-actin or Hoechst 33258 stock solution was prepared in anhydrous DMSO or PBS and stored at -20 °C. For labeling, 3D-cultured cancer cell spheroids were collected, and the SiR-actin or Hoechst 33258 stock solution was diluted to 500 nM in culture medium. The cells were then incubated at 37 °C with 5% CO_2 for 1 hour, with the incubation time adjustable based on the staining outcome. For cell lines with high levels of efflux pump expression, the addition of 10 μM Verapamil to the staining solution may improve the staining quality. After incubation, imaging was performed using a live-cell workstation with a spinning-disk confocal microscope. The laser wavelength was

set to 640 nm (100 mW) with 20% laser intensity and an exposure time of 200 ms.

Live cell imaging. For 3D imaging, we established a live cell imaging platform by integrating a 3-gas controller (Oko-lab, 3GF-MIXER-HYPOXIA) and a temperature incubator (Oko-lab, H301-MINI) onto a spinning disk confocal microscope (SpinSR, Evident Olympus). The microscope incubators maintain a temperature of 37°C for live cell culture, while the gas controller regulates the flow rates of air, carbon dioxide, and nitrogen to maintain a carbon dioxide concentration of 5% and an oxygen concentration of either 21% or 2%, depending on experimental requirements. Cell samples in confocal dish (Nest, 801001) were placed on the live cell workstation. Typically, we set the laser intensity to 20% and the exposure time to 200 ms. To capture the dynamics of tumor spheroids, we utilized a laser with a wavelength of 488 nm to image the cytoskeleton and a laser with a wavelength of 561 nm to image the nuclei. To capture cell cycle , the 488 nm laser was used to image nuclei in the S/G2/M phases, while the 561 nm laser was employed to image nuclei in the G1 phase [91] To enhance experimental throughput, we selected a quad-well confocal dish (Cellvis, D35C4-20-1.5-N) for imaging, where each well operates independently without interference. Typically, three imaging positions are chosen within each well. When imaging 3D samples, at each position, a total 60 μm range along the z-axis was scanned at an interval of 5 μm, resulting in a total number of 15 images for one stack. When imaging 2D samples, images are captured at each position along the Z-axis at 3 μm intervals, resulting in a total of 7 images for one stack and a total z-range of 18 μm. The super-resolution images are obtained under the corresponding mode of the spinning disk confocal microscopy, using a 60x objective. Images were captured every hour for a total duration of 42 hours, with no significant phototoxicity observed [92-94].

Data reconstruction and 3D visualization. The reconstruction of imaging stacks from confocal microscopy is conducted using Cell Sens Dimension Desktop 4.2.1 [95]. In the top planer view, the Maximum Intensity Projection (MIP) algorithm is adopted to overlay all images in the z-stack into a single image. In the side view, the Marching Cubes (Surface Reconstruction Algorithms) algorithm is used to yield the stereoscopic spheroids.

Analysis of live cell imaging data. To analyze the spheroid, we segmented the tumor spheroids using CellPose [96], which provided the mask file of the spheroids. XY coordinates of each point on the spheroid's edge are then calculated based on the mask data. Subsequently, using the segmentation data, we employed custom-written MATLAB code to analyze dynamic parameters, including area, perimeter, circularity, movement direction, and size of the tumor spheroids. Time-series image stacks were imported into ImageJ. The Tracking Plugin Manual Tracking [97] was utilized to obtain the movement trajectories, centroid spatial coordinates, distance, and speed of the tumor spheroids. To give a closer look into cells, we first segment the cells for one imaging using CellPose 2.0 [98], determining the optimal input parameters. Then, we utilized home-built Python code to perform batch segmentation for a series of image stacks. Once the batch-processed data were obtained, we re-imported them into CellPose for fine-tuning for segmentation parameters and obtaining the mask data of the cells. After acquiring the cell edge coordinates from the mask data, we employed home-built MATLAB scripts to analyze various properties of the cells, including centroid coordinates, area, roundness, fluorescence intensity, motility, and direction. Subsequently, statistical analysis and visualization were performed using OriginLab and ImageJ, respectively.

Transcriptome sequencing and analysis. The tumor spheroids cultured in three dimensions are embedded in the matrix gel and cannot be separated individually. Therefore, when extracting RNA from these three-dimensional tumor spheres, we directly added Trizol into the matrix gel containing the tumor spheroid for extraction [99]. In contrast, cells cultured in two dimensions can be lysed directly using Trizol. After culturing cancer cell spheroids under normoxia or hypoxia conditions for 42 hours, the culture medium was aspirated,

and TransZol (TransGen, ET101-01-V2) was added directly to the mixture containing matrix gel and cells. RNA was then extracted and purified using the EasyPure® RNA Kit (TransGen, ER501-01-V2). The purified RNA was sent to Beijing Genomics Institution for library construction and sequencing, yielding sequencing data [100]. We subsequently utilized R packages and Galaxy [101] to align the sequencing data with human genomic information. To elucidate patterns and regulatory mechanisms of gene expression, regular analyses have been conducted, including sequence alignment, gene expression quantification, and differential expression analysis, Furthermore, we conducted GO and KEGG enrichment analyses of differentially expressed genes to gain deeper insights into the molecular mechanisms and regulatory networks underlying biological processes.

Laser ablation experiments. To assess the mechanical property of tumor spheres, we employed a high-power laser to ablate individual cells within the tumor spheroids and monitored the response [102]. Tumor spheroids cultured were first placed under a confocal microscope. Before laser ablation, ensure that tumor spheroids in different samples were at comparable z0 heights and had similar sizes. The intensity of the 405 nm laser was set to 100 % (50 mW), with a duration of 10 seconds for each ablation. A single cell at the edge of the tumor sphere was randomly selected for ablation. After laser exposure 4-5 times, the selected cell was ablated. During the ablation process, real-time imaging of the actin was conducted using a 488 nm laser, allowing for simultaneous live cell recording. Subsequent analysis focused on the deformation of the tumor spheroids over time.

Nano-identation measurements. The nano-indentation instrument (PIUMA Chiaro) can characterize the Young's modulus of cell surfaces with high precision without deconstructing the cells [103]. We measured the Young's modulus of cell surfaces under both hypoxia and normoxia conditions. The sample preparation method was identical to that used for two-dimensional live-cell imaging. The confocal dish was placed under the microscope when the cell density reached approximately 70-80%. We first observe the sample under the objective, placing the interested cell at the center of view field. Then a nanoindentation probe with the size of 2 μm is lowered onto the cell surface, giving feedback to the *in situ* force it senses. Nine random locations were selected on each confocal dish for measurement with the same nanoindentation probe.

72. Sodunke, T. R. *et al.* Micropatterns of Matrigel for three-dimensional epithelial cultures. *Biomaterials* **28**, 4006-4016 (2007).
73. Braun, F. K. *et al.* Scaffold-Based (Matrigel™) 3D Culture Technique of Glioblastoma Recovers a Patient-like Immunosuppressive Phenotype. *Cells* **12** (2023).
74. Flatau, G. *et al.* Toxin-induced activation of the G protein p21 Rho by deamidation of glutamine. *Nature* **387**, 729-733 (1997).
75. Tokic, S. *et al.* The RhoA guanine exchange factor ABR: a glucose-sensitive mediator of actin reorganization in feto-placental arterial endothelial cells altered by gestational diabetes mellitus. *J Physiol* (2024).
76. Bito, H. *et al.* A critical role for a Rho-associated kinase, p160ROCK, in determining axon outgrowth in mammalian CNS neurons. *Neuron* **26**, 431-441 (2000).
77. Isler, D. *et al.* Antitumoral effect of a selective Rho-kinase inhibitor Y-27632 against Ehrlich ascites carcinoma in mice. *Pharmacol Rep* **66**, 114-120 (2014).
78. Riedl, J. *et al.* Lifeact: a versatile marker to visualize F-actin. *Nat Methods* **5**, 605-607 (2008).
79. Mannan, T., Jing, S., Foroushania, S. H., Fortune, F. & Wan, H. RNAi-mediated inhibition of the desmosomal cadherin (desmoglein 3) impairs epithelial cell proliferation. *Cell Prolif* **44**, 301-310 (2011).
80. Shan, G. RNA interference as a gene knockdown technique. *Int J Biochem Cell Biol* **42**, 1243-1251 (2010).
81. Cai, F. *et al.* Desmoglein-2 is overexpressed in non-small cell lung cancer tissues and its knockdown

suppresses NSCLC growth by regulation of p27 and CDK2. *J Cancer Res Clin Oncol* **143**, 59-69 (2017).
82. Miller, P. G. *et al.* In Vivo RNAi screening identifies a leukemia-specific dependence on integrin beta 3 signaling. *Cancer Cell* **24**, 45-58 (2013).
83. Kovacheva, M., Zepp, M., Berger, S. & Berger, M. R. Conditional knockdown of integrin beta-3 reveals its involvement in osteolytic and soft tissue lesions of breast cancer skeletal metastasis. *J Cancer Res Clin Oncol* **147**, 361-371 (2021).
84. Hu, H. J. *et al.* Integrin beta 3-overexpressing mesenchymal stromal cells display enhanced homing and can reduce atherosclerotic plaque. *World J Stem Cells* **15**, 931-946 (2023).
85. *About GeneChem*, <https://www.genechem.com.cn/about.html >
86. Mayr, S. *et al.* Localization Microscopy of Actin Cytoskeleton in Human Platelets. *Int J Mol Sci* **19** (2018).
87. Yu, Z. *et al.* Targeting UBR5 inhibits postsurgical breast cancer lung metastases by inducing CDC73 and p53 mediated apoptosis. *Int J Cancer* **154**, 723-737 (2024).
88. Liu, J. *et al.* Tanshinone IIA promotes apoptosis by downregulating BCL2 and upregulating TP53 in triple-negative breast cancer. *Naunyn Schmiedebergs Arch Pharmacol* **396**, 365-374 (2023).
89. Bazhulina, N. P. *et al.* Binding of Hoechst 33258 and its derivatives to DNA. *J Biomol Struct Dyn* **26**, 701-718 (2009).
90. Lukinavičius, G. *et al.* Fluorogenic probes for live-cell imaging of the cytoskeleton. *Nat Methods* **11**, 731-733 (2014).
91. Sakaue-Sawano, A. *et al.* Visualizing spatiotemporal dynamics of multicellular cell-cycle progression. *Cell* **132**, 487-498 (2008).
92. Gintoli, M. *et al.* Spinning disk-remote focusing microscopy. *Biomed Opt Express* **11**, 2874-2888 (2020).
93. Ewald, A. J., Werb, Z. & Egeblad, M. Dynamic, long-term in vivo imaging of tumor-stroma interactions in mouse models of breast cancer using spinning-disk confocal microscopy. *Cold Spring Harb Protoc* **2011**, pdb.top97 (2011).
94. Hayashi, S. & Okada, Y. Ultrafast superresolution fluorescence imaging with spinning disk confocal microscope optics. *Mol Biol Cell* **26**, 1743-1751 (2015).
95. *cellSens*, <https://lifescience.evidentscientific.com.cn/en/software/cellsens/>
96. Stringer, C., Wang, T., Michaelos, M. & Pachitariu, M. Cellpose: a generalist algorithm for cellular segmentation. *Nat Methods* **18**, 100-106 (2021).
97. *Manual Tracking*, <https://imagej.net/ij/plugins/track/track.html>
98. Pachitariu, M. & Stringer, C. Cellpose 2.0: how to train your own model. *Nat Methods* **19**, 1634-1641 (2022).
99. Ferretti, R. *et al.* Tumor cell invasion into Matrigel: optimized protocol for RNA extraction. *Biotechniques* **70**, 327-335 (2021).
100. Kim, H. M. *et al.* Comparative analysis of 7 short-read sequencing platforms using the Korean Reference Genome: MGI and Illumina sequencing benchmark for whole-genome sequencing. *Gigascience* **10** (2021).
101. *Galaxy*, <https://usegalaxy.cn/>
102. Lele, T. P., Thodeti, C. K. & Ingber, D. E. Force meets chemistry: analysis of mechanochemical conversion in focal adhesions using fluorescence recovery after photobleaching. *J Cell Biochem* **97**, 1175-1183 (2006).
103. Qian, L. & Zhao, H. Nanoindentation of Soft Biological Materials. *Micromachines (Basel)* **9** (2018).

Acknowledgments: We thank Min Bao for helpful discussions; Ruirui Gao and Yeqing Leng for sharing monoclonal transfected cell lines; and ChatGTP for text polishing. This study was supported by taxpayers of China through National Natural Science Foundation of China (distinguished young scholars funding, overseas) and Wuhan Univerisity (talents startup funding).

Author contributions. B.L. conceptualized the project, B.L. Z. D.W. designed the research and performed experiments. Z. D.W. analyzed the data with the help of L.T. All authors discussed the results and wrote the paper.

Competing interests. The authors declare no competing interests.

Additional information

Extended data is available for this paper after the main text.

Supplementary information is available for this paper at a separate file.

Reprints and permissions information are available at

Correspondence and requests for materials should be addressed to B. L. (libo@whu.edu.cn)

Data availability The data and analysis code that support the findings of this study are submitted with the paper by separate files.

Figure Caption

Figure 1. Hypoxia promotes early tumorigenesis by active fusion. a, Confocal images of HEK293T cells cultured in 3D Matrigel under 21% oxygen (left) and 2% oxygen (right) for 42 hours. The images are the typical reflection of more than three independent experiments. The green and red channels are LifeAct and H2B, respectively. The scale bar is 100 μm. **b,** Cell number, maximum cross-sectional area of tumor spheroids, and total number of spheroids after 48 hours of 3D culture. **c,** Tumorigenesis rate of HEK293T cells under different conditions of normoxia, hypoxia andPHAi treatments. The shaded area in the first two columns represents the parts of tumorigenesis contributed by growth. **d,** Fusion frequency of tumor spheroids under different culture conditions. **e,** Time required for the active fusion under different culture conditions of normoxia, hypoxia, PHAi, and RNAi treatments. **f,** Proportion of active and growth modes in the fusion under different culture conditions of normoxia, hypoxia, PHAi, and RNAi treatments. **g-j**, Representative confocal images of more than three independent experiments that reflect the tumor spheroids fusion under different culture conditions. The left panels are images taken at 0 hours and the right panels are taken at 42 hours after the treatment. Compared with the normal 21% oxygen control (**g**), active fusion is promoted under 2% hypoxia condition (**h**) or Rho activator II treatment (**i**). The active fusion under hypoxia disappears after Y-27632 treatment (**j**) Green and red channels are LifeAct and H2B, respectively. The scale bar is 20 μm. **k-n,** Time evolution of maximum cross-sectional area, fusion frequency, cell number, and speed of the spheroids under conditions of 21% Oxygen (**k**), 2% Oxygen (**l**), 21% Oxygen with Rho Activator II (**m**), and 2% Oxygen with Y-27632 (**n**). **o, p,** Standard deviation of the spheroid speed (**o**) and maximum cross-sectional area (**p**) across different culture conditions. For all statistical plots, unpaired Student's t-test ($n > 3$ experiments, data are mean ± SEM) was conducted for all data with **** $P < 0.0001$, *** $P < 0.001$, ** $P < 0.1$, * $P < 0.5$, ns $P > 0.5$. The error bars are the standard error of the mean of the data.

Figure 2. Dynamics of the tumor spheroids during the active fusion. a-d, Typical trajectories of tumor spheroids in 24 hours under different culture conditions of normal 21% oxygen (**a**), 2% hypoxia (**b**), Rho-activate II treatment under normoxia (**c**), and Y-27632 treatment under hypoxia (**d**). The data is a typical reflection of three independent experiments. The colors represent different tumor spheroids. **e**, Speed in 3-dimension of tumor spheroids under different culture conditions of normoxia, hypoxia, PHAi, and RNAi treatment. **f**, The distance between the non-fused tumor spheres and their initial positions over time under various conditions of normoxia, hypoxia, PHAi, and RNAi treatment. **g,** The distance between two tumor spheroids before active fusion occurs under various conditions of normoxia, hypoxia, PHAi, and RNAi treatment. **h-k,** Typical trajectories of two fusing tumor spheroids under various conditions of 21% normal oxygen (**h**), 2% hypoxia (**i**), normoxia treated with Rho-activate II (**j**) and hypoxia treated with Y-27632 (**k**). The data is a typical reflection of three independent experiments. The dashed and solid vectors represent the trajectory of the two spheroids each. The direction and length of the vectors indicate the movement direction and speed of the spheroids at each time point, respectively. The color represents the time. **l**, Circularity of the tumor spheroid during active fusion under different culture conditions. **m,** Time evolution of the tumor spheroid circularity during the active fusion under various culture conditions of normoxia, hypoxia, PHAi, and RNAi treatments. **n,** Degree of deformation of the tumor spheroid after laser ablation under different culture conditions of 21% normal oxygen, 2% hypoxia, normoxia treated with Rho-activate II, and hypoxia treated with Y-27632. The wavelength of the laser is 405 nm and the power of ablation is 50 mW. For all statistical plots, unpaired Student's t-test ($n > 3$ experiments, data are mean ± SEM) was conducted for all data with **** $P < 0.0001$, *** $P < 0.001$, ** $P < 0.1$, * $P < 0.5$, ns $P > 0.5$. The error bars are the standard error of the mean of the data.

Figure 3. Tiny nucleus and outreaching F-acting guide the active fusion. a-d, Typical confocal images

from more than three independent experiments of tumor spheroid composed of HEK293T-FUCCI cells in 3D culture for 42 hours under 2% oxygen conditions. The cells are labeled with FUCCI, in which the color indicates different stages of the cell cycle. - Red marks hCdt1, indicating cells are in the G1 phase, and green marks hGem, indicating cells are in the S/G2/M phases. The white dotted circle indicates the nucleus of the tiny cells. The scale bar is 10 μm. **e,** Probability distribution of nucleus sizes under different 3D culture conditions of normoxia, hypoxia, normoxia treated with Rho-activate II, and hypoxia treated with Y-27632. **f,** Immunostaining of DAPI confirms that the nucleus of tiny cells contains chromosome materials. The dashed white circles indicate the tiny cells. **g,** Relative changes in the number of tiny and normal nuclei over the same period of 42 hours. **h, i,** Typical immunostaining images of the tumor spheroids taken by 40x objective (**e**) and 128x super resolution mode (**i**) under normoxia conditions. The green channel is F-actin, the red is H2B and the blue channel is Hoechst. **j,** A representative confocal immunostaining image showing the outreaching F-actin that bridge two fusing tumor spheroids. The dashed white circles indicate the outreaching F-acting structure. **k,** The length of out-reaching F-actin from the spheroid surface in normoxia and hypoxia conditions. **l,** Time evolution of the F-actin bridge length, the distance between the spheroid and the spheroids' speed during active fusion. **m-o,** Confocal images of HEK293T-FUCCI tumor spheroids during the active fusion process. The tiny cells appear at the proximal gap between the two spheroids during the fusion (**n**) but are not observed before (**m**) and after (**o**). The white arrow in **n** indicates the nucleus of the tiny cells. The green and red channels are hCdt1 and hGem, respectively. The scale bar in **h, j** is 20 μm, and the scale bar in **i** is 10 μm. The images are typical reflection of three independent experiments. **p,** Probability distribution of the distance ("D" in the **inset**) between the tiny and normal cells the center of tumor spheroids during active fusion. A distance of 1 indicates positioning at the spheroid's edge. The **inset** of **p** schematically demonstrates the relative positions between the tiny cells and the spheroids. **q,** Probability distribution of the angle ("θ" in the **inset** of **p**) between the tiny cell nucleus–spheroid center axis and the spheroid center-spheroid center axis during the active fusion. A smaller θ value means a closer location to proximal ends of the axis that connects the mass centers of the two spheroids. The **inset** of **q** is the enlarged part of the gap region between two fusing spheroids. The white arrow indicates the nucleus of the tiny cells. **r,** Speed of tiny and large nuclei in cells. For all statistical plots, unpaired Student's t-test ($n > 3$ experiments, data are mean ± SEM) was conducted for all data with **** $P < 0.0001$, *** $P < 0.001$, ** $P < 0.1$, * $P < 0.5$, ns $P > 0.5$. The error bars are the standard error of the mean of the data.

Figure 4. Hypoxia promotes spheroid growth in 3D by modulating the cell cycle. a, Representative Confocal images of tumor spheroid under 21% oxygen (left) and 2% oxygen (right) conditions after 42 hours of 3D culture. The images are the typical reflection of more than three independent experiments. The green and red channels are LifeAct and H2B, respectively. The scale bar is 10 μm. **b,** Proliferation rate of HEK293T cells under different 3D culture conditions of normoxia, hypoxia, and PHAi experiments. **c,** Proportion of HEK293T cells in the S/G2/M phases under different 3D culture conditions of normoxia, hypoxia, and PHAi experiments. **d-g,** Typical confocal images of tumor spheroids composed of HEK293T-FUCCI cell line under various culture conditions of normoxia control (**d**), hypoxia (**e**), normoxia with Rho-activate II treatment (**f**) and hypoxia with Y-27632 treatment (**g**). The upper column is images taken at 0 hours and the lower column is images taken at 42 hours. The green and red channels are hCdt1 and hGem, respectively. The scale bar is 20 μm. **h-k,** Proportion of cells in G1 phase (h) or S/G2/M phases as a function of time normoxia (**h**), hypoxia (**i**), normoxia with Rho-activate II treatment (**j**), and hypoxia with Y-27632 treatment (**k**). (**l-n**) Typical immunostaining images showing p53 expression in the spheroids under normoxia (**l**) and hypoxia (**m, n**) culture conditions. Green fluorescence indicates p53, and blue fluorescence marks cell nuclei. The scale bar represents 20 μm. (**o**) Proportion of p53-positive cells with nuclear localization in tumor spheroids under different culture conditions. (**p**) Proportion of cells with p53 nuclear localization in regular and tiny cells under hypoxic culture conditions. For all statistical plots, unpaired Student's t-test ($n > 3$ experiments, data are mean

± SEM) was conducted for all data with **** P < 0.0001, *** P < 0.001, ** P < 0.1, * P <0.5, ns P > 0.5. The error bars are the standard error of the mean of the data.

Extended Date Figure 1. Schematics of the experimental design and workflow of this study. In the sample preparation stage, lentivirus is used to construct cell lines expressing target proteins with fluorescent tags. The cells are seeded into a three-dimensional matrix gel network, and spheroids are allowed to form over 24 hours. Live-cell imaging is then performed on the integrated platform composed of a spinning disk confocal microscope and a three-gas incubator. The whole dynamical processes over extended periods are recorded under various oxygen concentrations with minimal phototoxicity. The obtained imaging data are processed by AI-based cell segmentation. The dynamic information of the tumor spheroid is extracted using homebuilt MATLAB codes and ImageJ plugin. Advanced molecular cell biology techniques, including transcriptomic sequencing and qPCR, are used to further elucidate the molecular mechanisms behind the dynamical phenotype.

Extended Date Figure 2. Comparison between the HEK293T cells in 3-dimensional and 2-dimensional cultures under hypoxia. a, Volcano plots of differentially expressed genes under 3D and 2D culture. Cancer-related genes are indicated by black arrows. **b-d,** KEGG enrichment analysis of differentially expressed genes on biological process (**b**), cellular component (**c**), and molecular function (**d**). The bubble plot illustrates the top ten representative results. The size of each bubble represents the number of genes involved, the color indicates the significance level (p-value). Data are from three independent experiments.

Extended Date Figure 3. Schematic summary of early tumorigenesis under normoxia and hypoxia conditions. The overall tumorigenesis is significantly promoted by hypoxia treatment due to the altered dynamical phenotype of the tumor spheroids, including the major contribution from active fusion and minor contribution from enhanced growth. At the cellular level, the active fusion is directed by the outreaching F-actin and tiny cells that bridge the gaps between the fusion spheroids. At the molecular level, cytoskeleton proteins and nucleus are optimized for the structural basis for the dynamics and mechanics of the tumor spheroids, leading to their proper biological function in adaptation to hypoxia.

Extended Date Figure 4. HEK293T in 2-dimensional culture under hypoxia conditions. a, Confocal images of HEK293T cells cultured under normoxia conditions (left) and hypoxia conditions (right) for 42 hours. The white lines indicate the borders of the cell colonies. The green and red channels are LifeAct and H2B, respectively. The scale bar is 100 μm. The images are representative ones from more than three independent experiments. **b,** Relative cell number changes 42 hours after seeding. **c,** Frequency of cell cluster fusion within ten hours under various culture conditions. **d,** Typical trajectories of HEK293T cell clusters under normoxia (left) and hypoxia (right) conditions in two-dimensional culture**. e,** Representative super-resolution images from 3 independent experiments of HEK293T cells under normaxia (left) and hypoxia (right) conditions in 2D culture. The scale bar is10 μm. The green fluorescence represents Phalloidin-labeled F-actin. The scale bar is 10 μm. **f,** Speed of HEK293T cells under different culture conditions in 2D. **g,** Quantification of cellular Young's modulus under normoxia or hypoxia culture conditions **h, i,** Confocal images of HEK293T-FUCCI cells from 3 independent experiments under nomoxia (**h**) and hypoxia (**i**) conditions in 2D culture. The left and right panels are images taken at 0 hours and 42 hours, respectively, after cell seeding. The green and red channels are hGem and hCdt1, respectively. The scale bar is 20 μm. **j, k,** Proportion of cells in G1 phase and S/G2/M phases under normoxia (**j**) or hypoxia (**k**) conditions as a function of time. **l,** Proportion of HEK293T cells in the S/G2/M phases under hypoxia and normoxia conditions in 2D culture. For all statistical plots, unpaired Student's t-test (n > 3 experiments, data are mean ± SEM) was conducted for all data with **** P < 0.0001, *** P < 0.001, ** P < 0.1, * P <0.5, ns P > 0.5. The error bars are the standard

error of the mean of the data.

Extended Date Figure 5. Differential analysis of 3-dimensional HEK293T transcriptomic data under hypoxia and normoxia conditions. a, KEGG biological process enrichment analysis of differentially expressed genes. The bubble plot shows the top ten enriched biological processes. **b,** KEGG pathway enrichment analysis of differentially expressed genes. The bubble plot shows the top ten KEGG pathways **c,** KEGG enrichment analysis of differentially expressed genes related to cytoskeletal dynamics. **d,** KEGG molecular function enrichment analysis of differentially expressed genes. For the KEGG plots in **a-d,** the size of each bubble represents the number of genes involved, while the color indicates the significance level (p-value). The mRNA samples are extracted from cells in 3-dimensional culture after 24 hours of 2% (hypoxia) or 20% (normoxia) oxygen treatment. All data are from three independent experiments.

Extended Date Figure 6. Outreach F-actin and tiny nucleus that bridges the gap between the fusing spheroids. a-d, Representative confocal images out of three independent experiments demonstrating the channels formed by outreaching F-actin between tumor spheroids under hypoxia conditions. The green channel is Phalloidin which labels F-actin, and the blue channel is Hoechst which labels nuclei. The scale bar is 20 μm. **e-h,** Representative time-lapse confocal images showing the formation of channels between two tumor spheroids through F-actin. Red fluorescence represents F-actin labeled with SiR-actin. The scale bar represents 20 μm. **i-l,** Representative confocal images out of three independent experiments demonstrating that the nuclei of the tiny cells locate between two fusing tumor spheroids under hypoxia conditions. The white arrows indicate the position of the tiny cells. The cells are labeled with FUCCI, in which the color indicates different stages of the cell cycle. - Red marks hCdt1, indicating cells are in the G1 phase, and green marks hGem, indicating cells are in the S/G2/M phases. The scale bar is 10 μm. **m-p,** Representative confocal images of tumor spheroids out of three independent immunostaining experiments proving that tiny cells contain chromosome materials. The cell nuclei are labeled with Hoechst. The white dotted circle indicates the tiny cells. The scale bar is 10 μm. **q,** Average area of nuclei inside and outside the channels formed by F-actin during tumor spheroid fusion. **r,** The angle between the long axis of cell nuclei and the direction of the channel itself. **s,** Ratio of the long axis length to the short axis length of cell nuclei inside and outside the F-actin channels. **t,** Probability distribution of nucleus sizes calculated from the immunostaining data under hypoxia and normoxia conditions in 3D control. For all statistical plots, unpaired Student's t-test ($n > 3$ experiments, data are mean ± SEM) was conducted for all data with **** $P < 0.0001$, *** $P < 0.001$, ** $P < 0.1$, * $P < 0.5$, ns $P > 0.5$. The error bars are the standard error of the mean of the data.

Extended Date Figure 7. Laser ablation confirms the role of outreaching F-actin and tiny cells in the active fusion. a-c, Representative confocal images showing the effects of laser ablation on micronuclei after culturing for 42 hours under normoxia conditions (**a**) or for 42 hours under 2% oxygen conditions (**b**), laser ablation followed by continued hypoxia culture for an additional 24 hours (**c**). The green fluorescence indicates F-actin labeled with phalloidin, while the blue fluorescence marks the nuclei with Hoechst. Scale bar = 50 μm. **d,** Quantification of tumor spheroid sizes under different culture conditions. **e-g,** Representative confocal images depicting the channels formed between two tumor spheroids after laser ablation following 42 hours of culture under normoxia conditions (**e**) or 42 hours under 2% oxygen conditions (**f**), and laser ablation then continued hypoxia culture for an additional 42 hours (**g**). The green fluorescence indicates F-actin labeled with phalloidin, while the blue fluorescence marks the nuclei with Hoechst. The scale bar is 50 μm. **h,** Quantification of tumor spheroid sizes under different culture conditions. For all statistical plots, unpaired Student's t-test ($n = 3$ experiments, data are mean ± SEM) was conducted for all data with **** $P < 0.0001$, *** $P < 0.001$, ** $P < 0.1$, * $P < 0.5$, ns $P > 0.5$. The error bars are the standard error of the mean of the data.

Figure 1

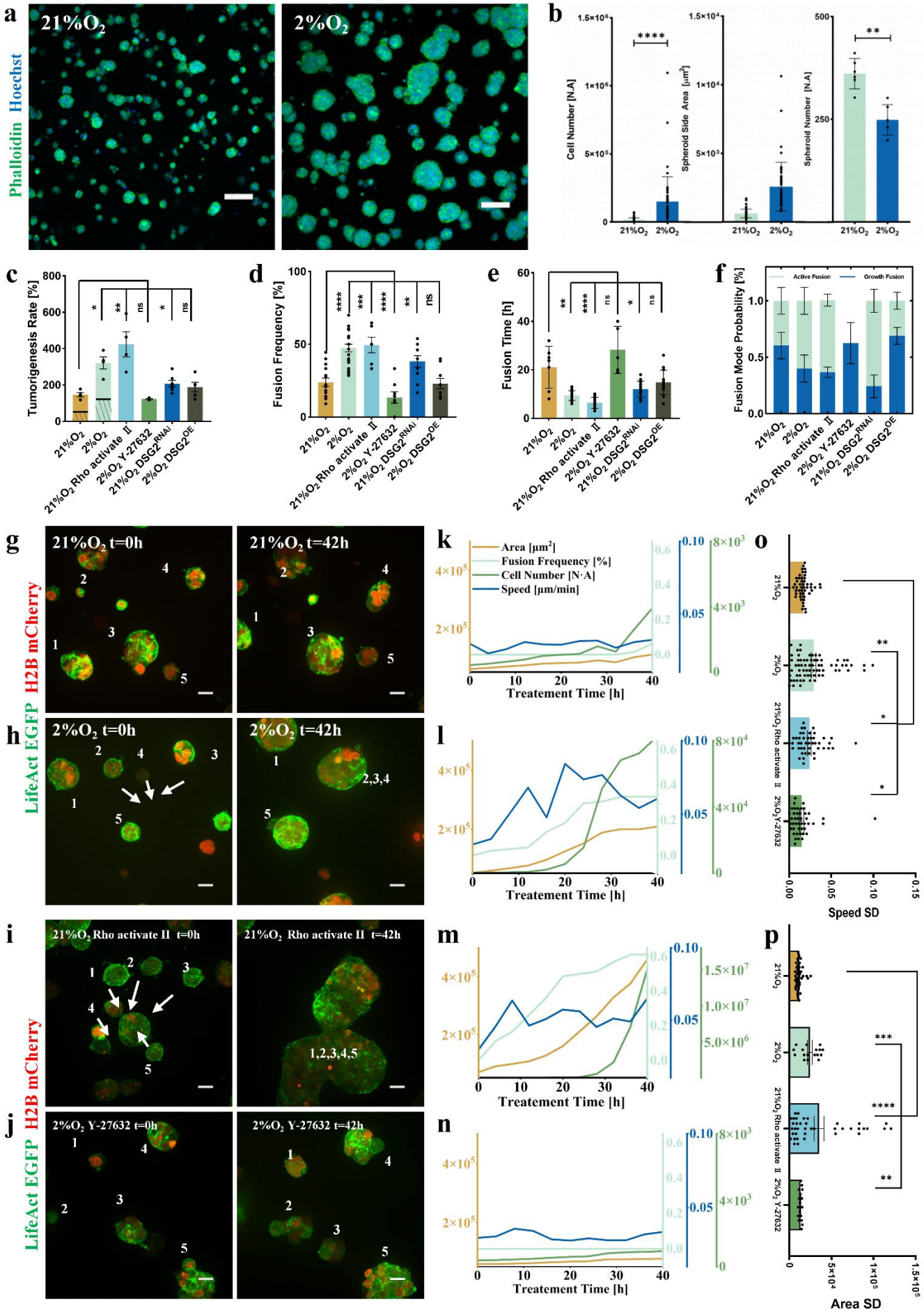
a
21%O2
2%O2
Phalloidin Hoechst
b
Cell Number [N.A]
Spheroid Side Area [μm²]
Spheroid Number [N.A]
c
Tumorigenesis Rate [%]
d
Fusion Frequency [%]
e
Fusion Time [h]
f
Fusion Mode Probability [%]
Active Fusion
Growth Fusion
21%O2
2%O2
21%O2 Rho activate II
2%O2 Y-27632
21%O2 DSG2RNAi
2%O2 DSG2OE
g
21%O2 t=0h
21%O2 t=42h
H2B mCherry
h
2%O2 t=0h
2%O2 t=42h
LifeAct EGFP
i
21%O2 Rho activate II t=0h
21%O2 Rho activate II t=42h
j
2%O2 Y-27632 t=0h
2%O2 Y-27632 t=42h
k
Area [μm²]
Fusion Frequency [%]
Cell Number [N·A]
Speed [μm/min]
Treatement Time [h]
l
m
n
o
Speed SD
p
Area SD

Figure 2

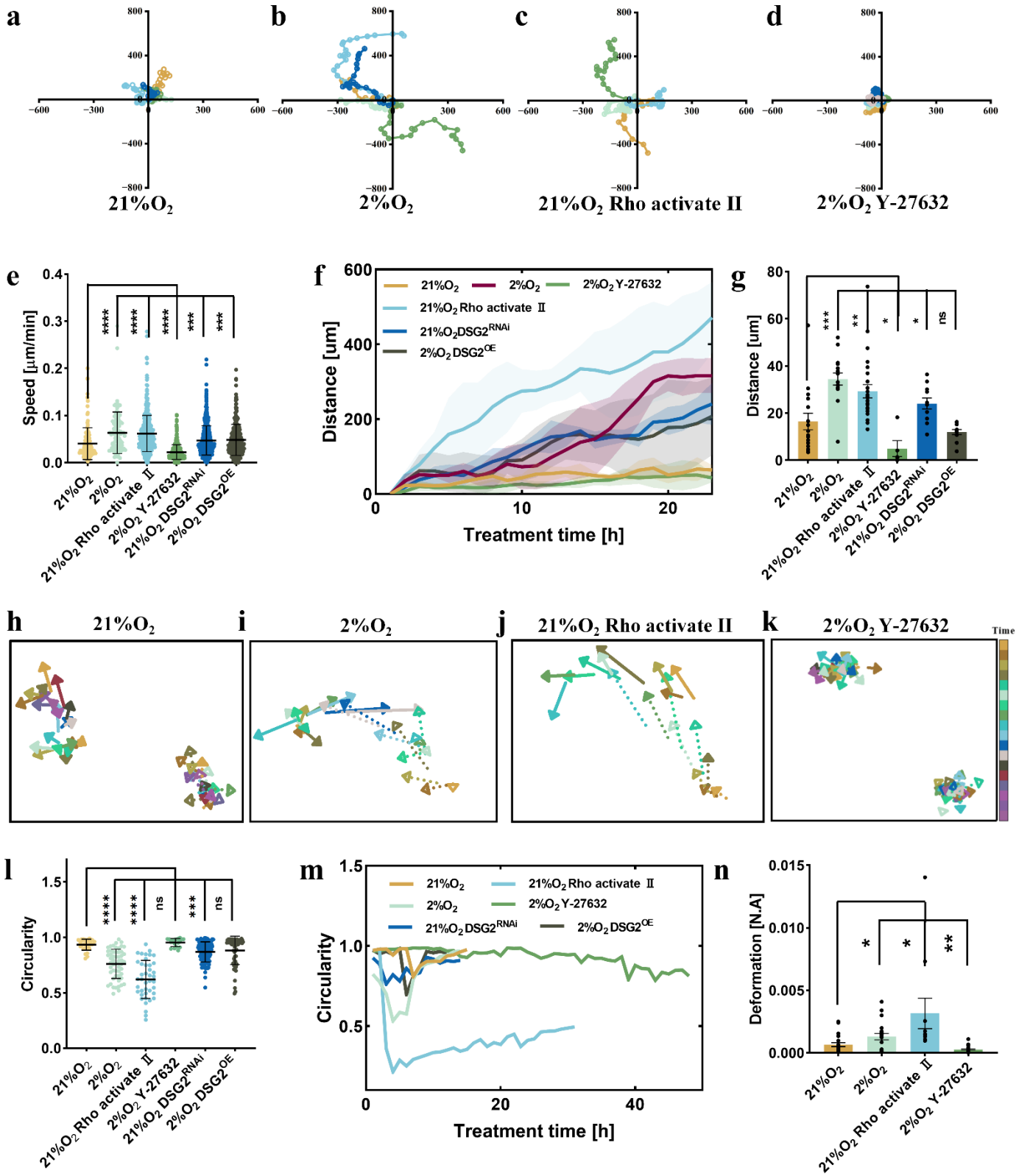
a
b
c
d
21%O2
2%O2
21%O2 Rho activate II
2%O2 Y-27632
e
Speed [μm/min]
f
Distance [um]
Treatment time [h]
21%O2
2%O2
2%O2 Y-27632
21%O2 Rho activate Ⅱ
21%O2DSG2RNAi
2%O2DSG2OE
g
Distance [um]
h
i
j
k
Time
l
Circularity
m
Circularity
Treatment time [h]
n
Deformation [N.A]

Figure 3

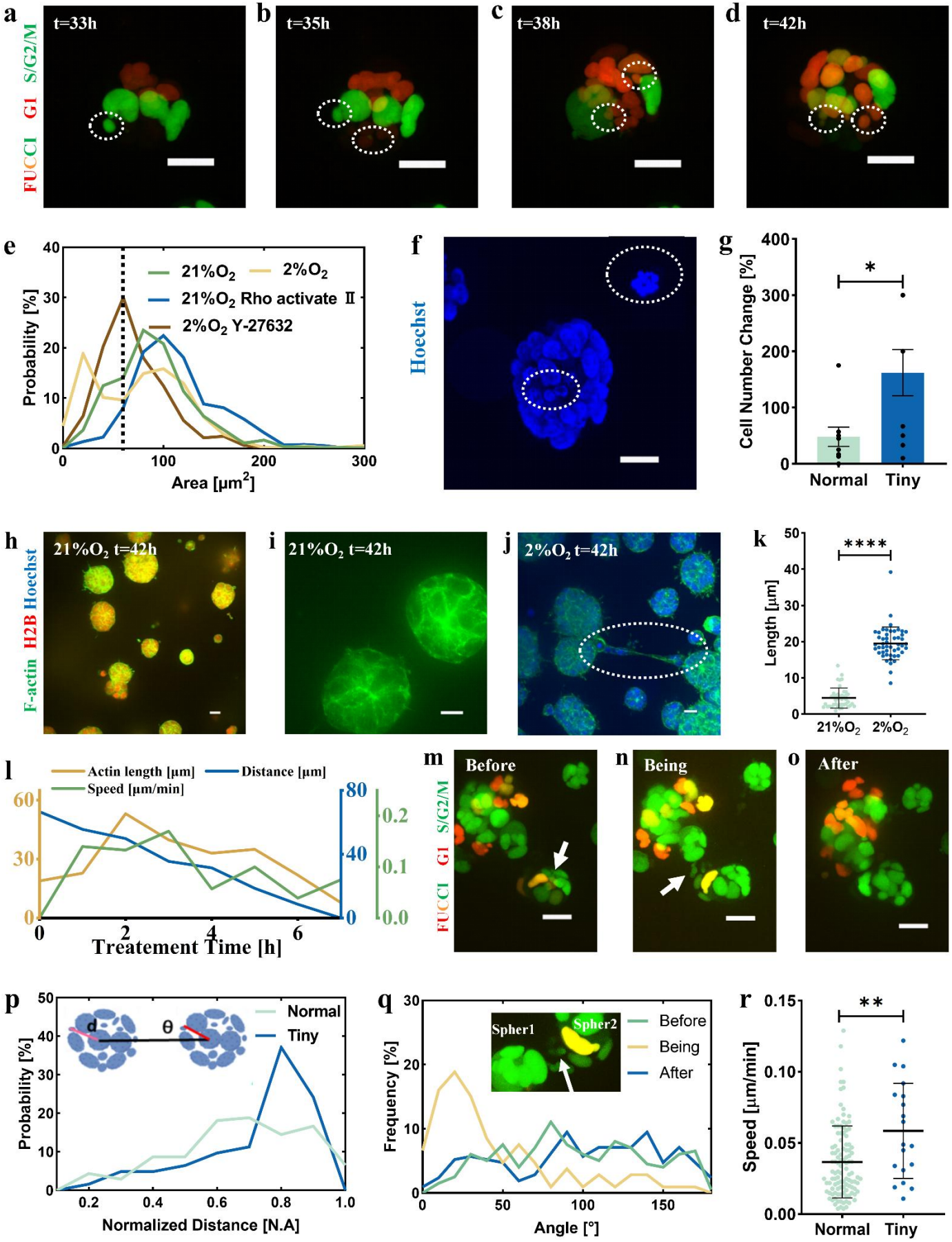
a
t=33h
b
t=35h
c
t=38h
d
t=42h
FUCCI G1 S/G2/M
e
Probability [%]
Area [μm²]
21%O₂
2%O₂
21%O₂ Rho activate Ⅱ
2%O₂ Y-27632
f
Hoechst
g
Cell Number Change [%]
Normal
Tiny
h
21%O₂ t=42h
F-actin H2B Hoechst
i
21%O₂ t=42h
j
2%O₂ t=42h
k
Length [μm]
21%O₂
2%O₂
l
Actin length [μm]
Distance [μm]
Speed [μm/min]
Treatement Time [h]
m
Before
n
Being
o
After
FUCCI G1 S/G2/M
p
Normal
Tiny
Probability [%]
Normalized Distance [N.A]
q
Spher1
Spher2
Before
Being
After
Frequency [%]
Angle [°]
r
Speed [μm/min]
Normal
Tiny

Figure 4

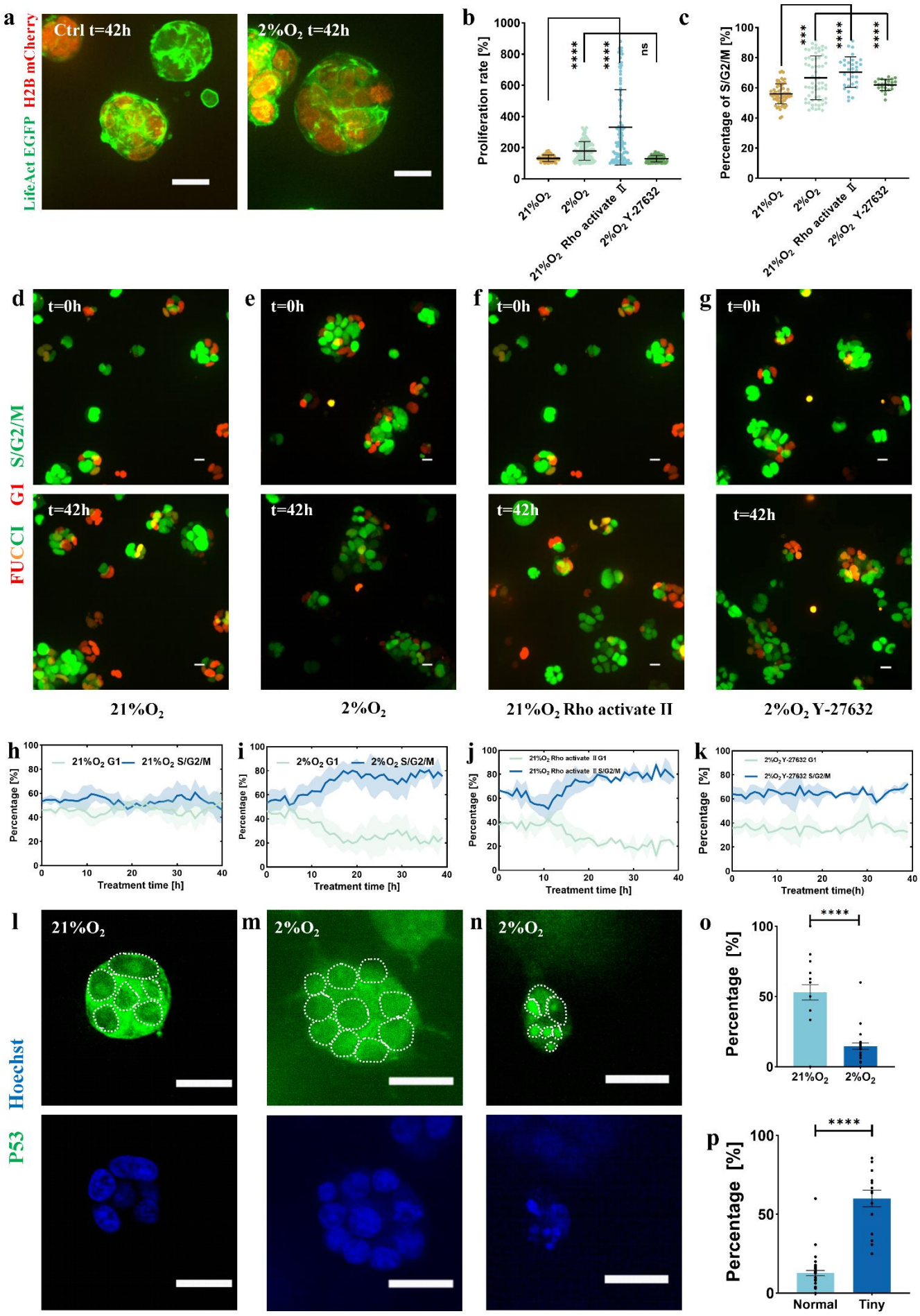
a
LifeAct EGFP H2B mCherry
Ctrl t=42h
2%O2 t=42h
b
Proliferation rate [%]
21%O2
2%O2
21%O2 Rho activate II
2%O2 Y-27632
c
Percentage of S/G2/M [%]
d
e
f
g
t=0h
t=42h
FUCCI G1 S/G2/M
21%O2
2%O2
21%O2 Rho activate II
2%O2 Y-27632
h
i
j
k
Percentage [%]
Treatment time [h]
21%O2 G1
21%O2 S/G2/M
2%O2 G1
2%O2 S/G2/M
21%O2 Rho activate II G1
21%O2 Rho activate II S/G2/M
2%O2 Y-27632 G1
2%O2 Y-27632 S/G2/M
l
m
n
o
p
Hoechst
P53
Normal
Tiny

Extended Date Figure 1

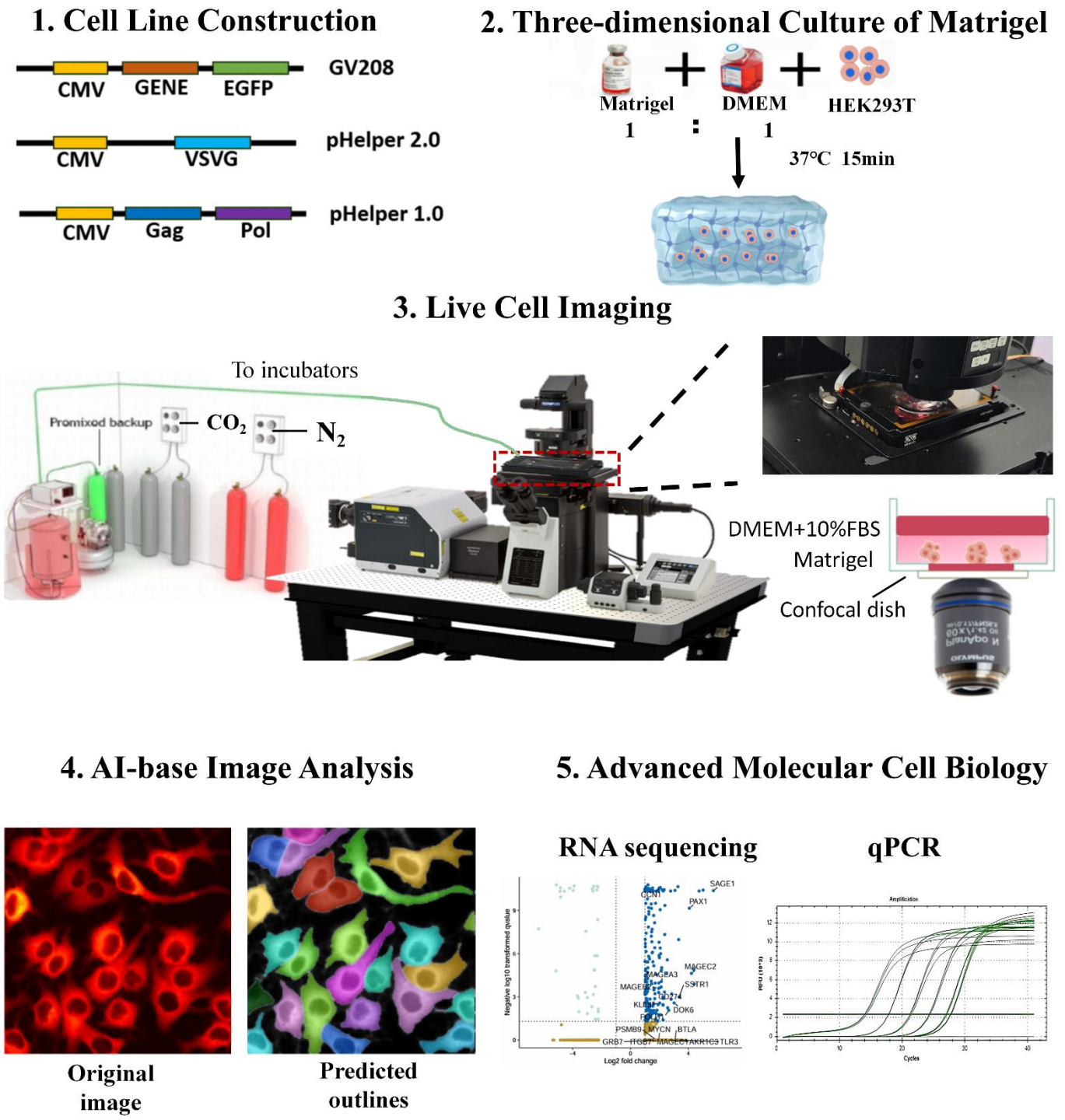

Extended Date Figure 2

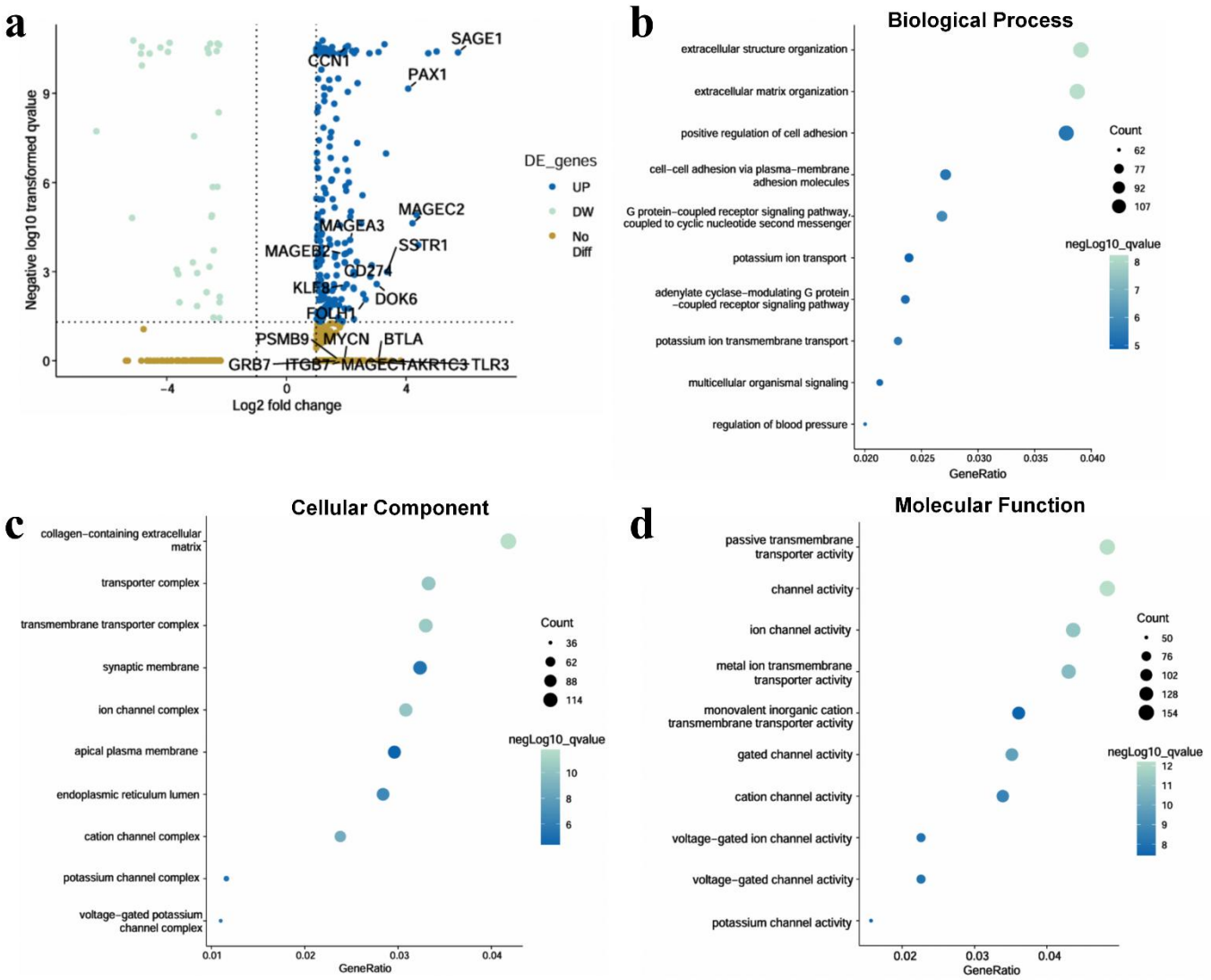

Extended Date Figure 3

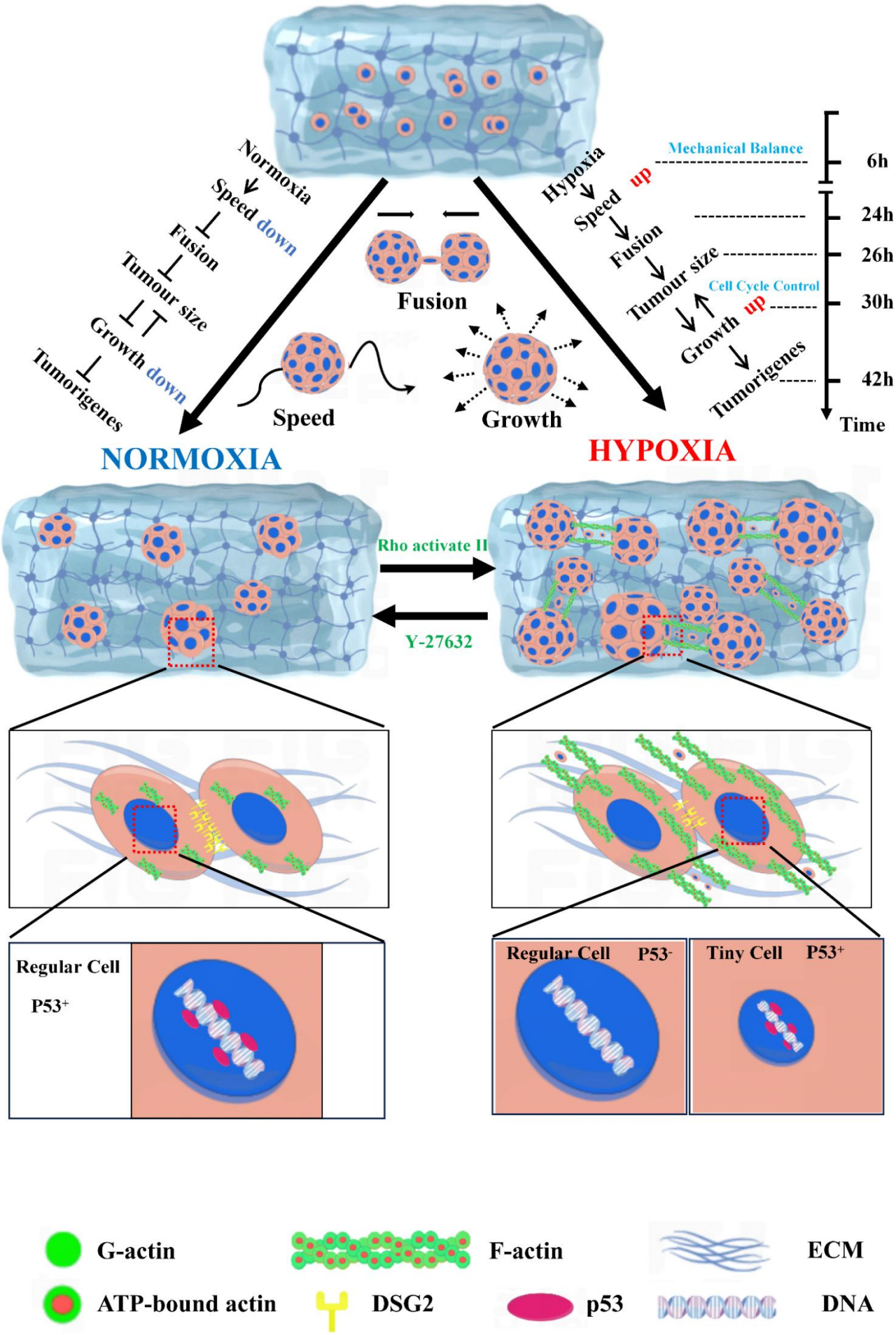

Extended Date Figure 4

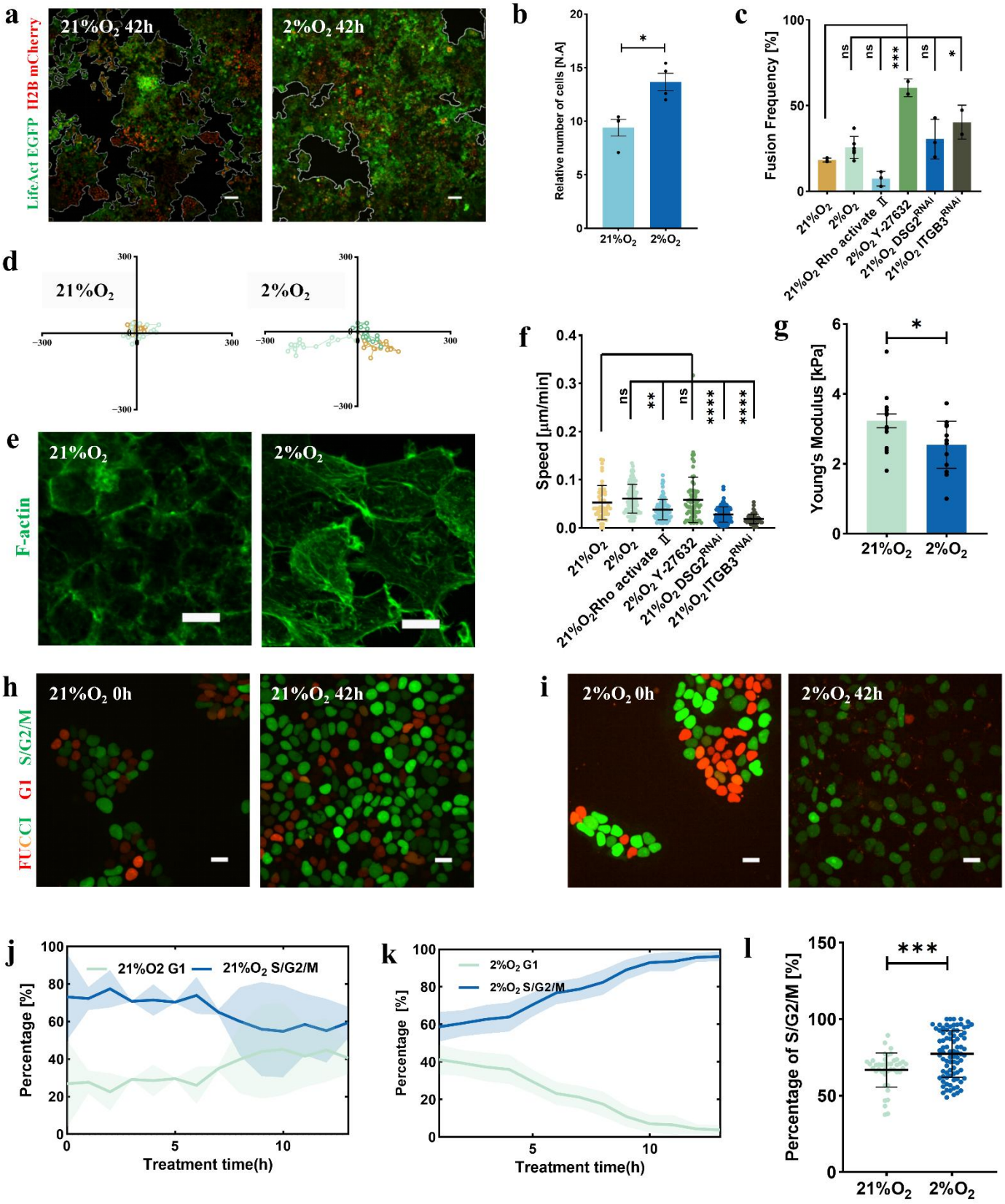

941 **Extended Date Figure 5**

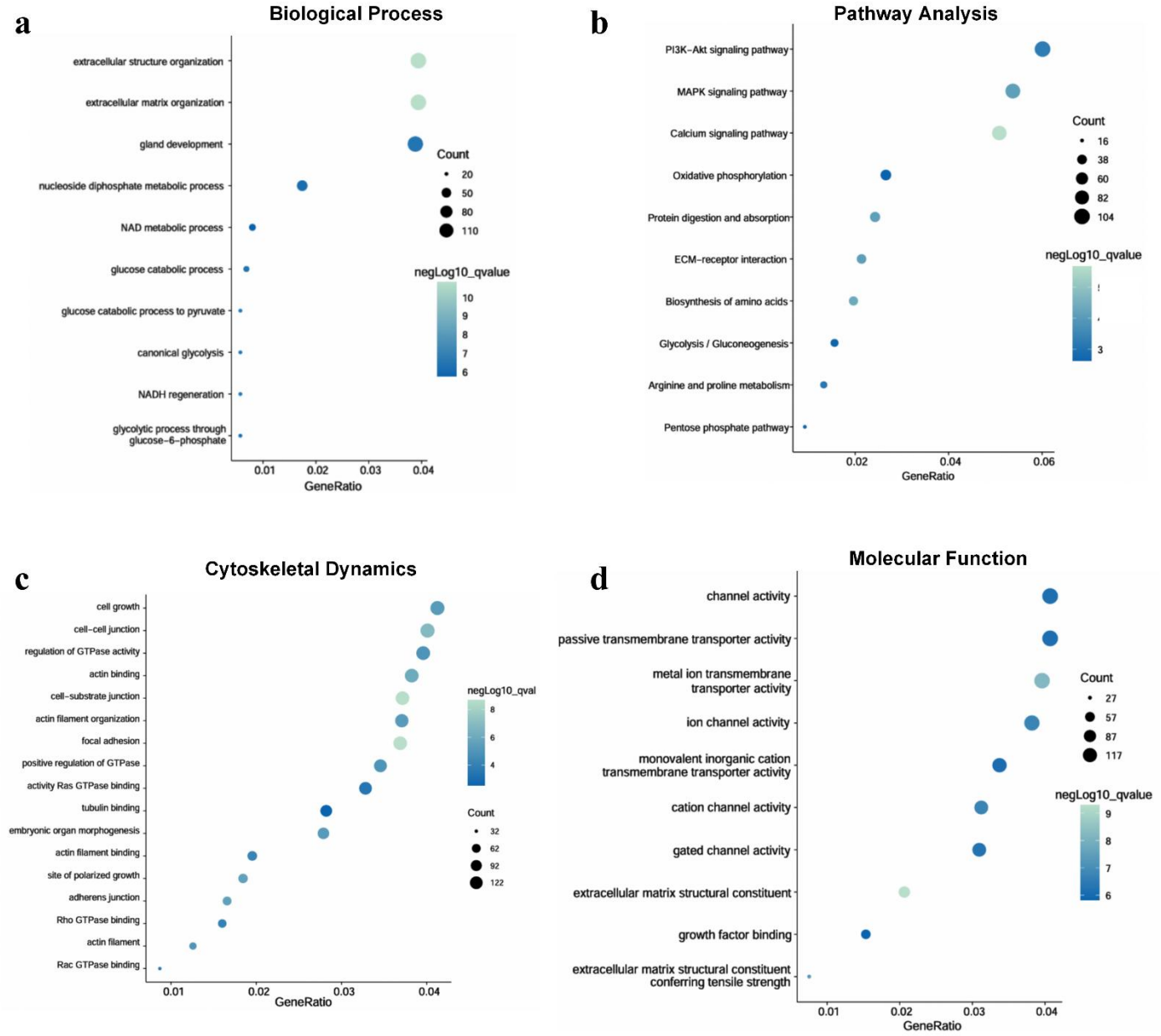

942

Extended Date Figure 6

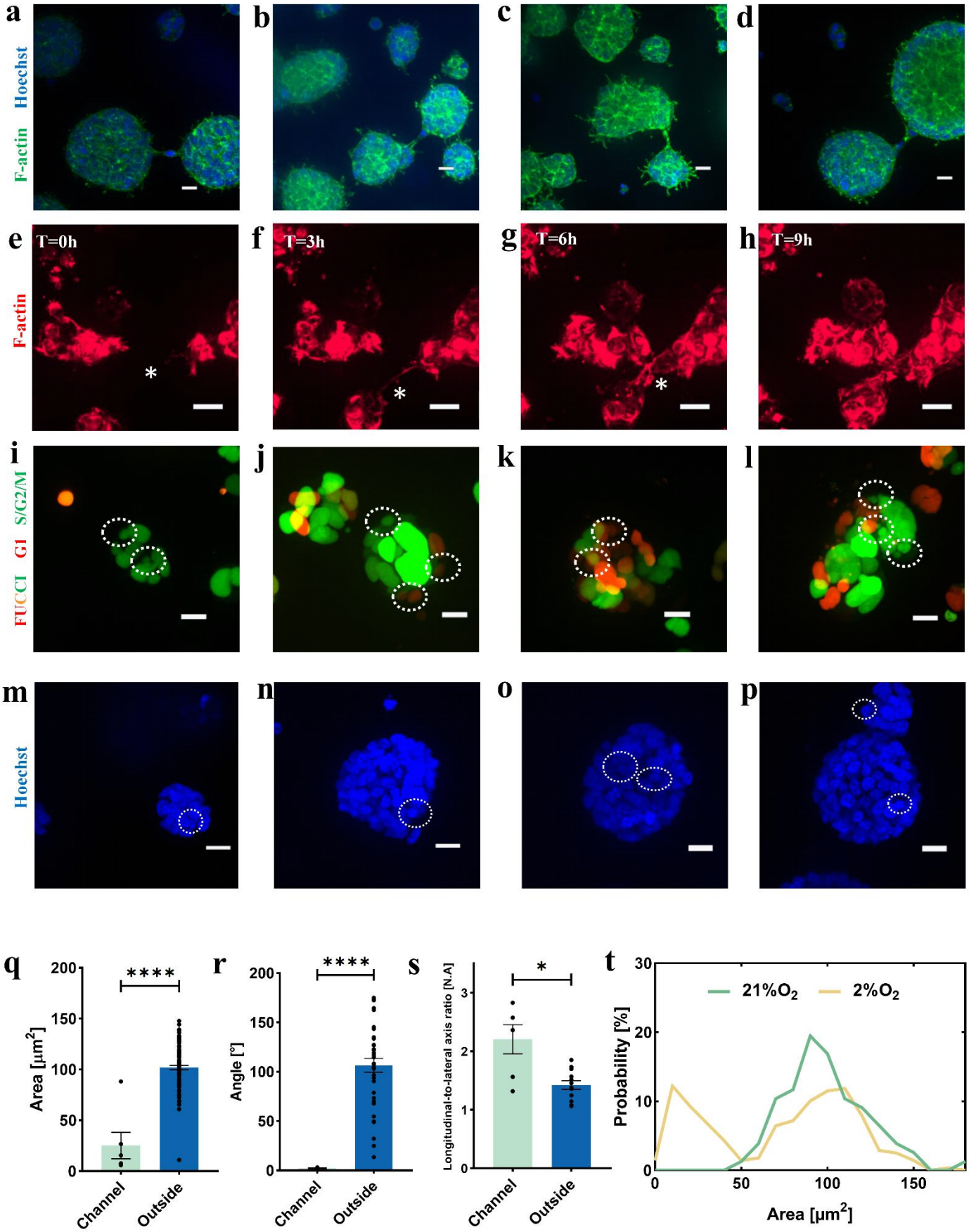
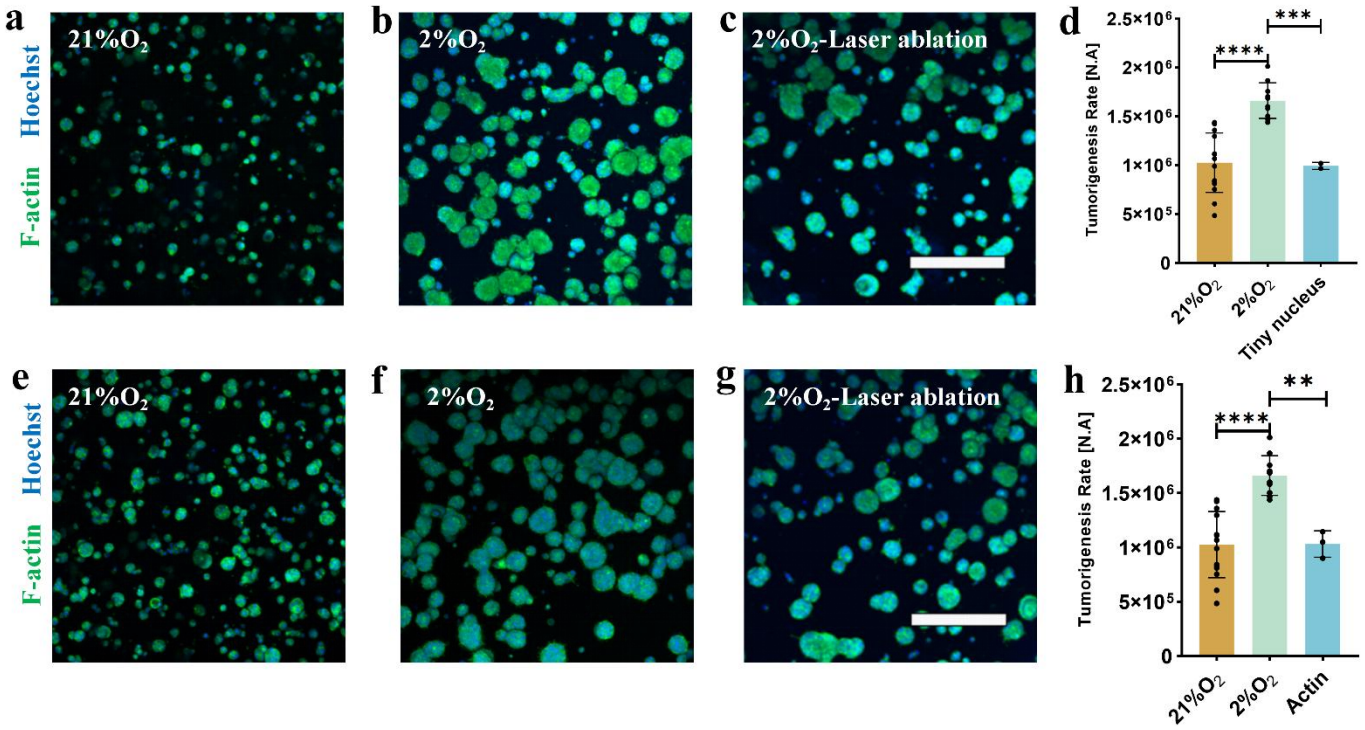
Extended Date Figure 7